DIMITRI Algorithm Theoretical Basis Document

Rayleigh Scattering Methodology for Vicarious Calibration

ESA contract: 4000114544/15/I-SBo

ARGANS Reference: ARG_DIM_QA4EO -TN-004b

Date: 26th September 2019

Version: 2.1

Authors

	NAME	AFFILIATION	CONTACT
Prepared by	B. Alhammoud	ARGANS Ltd, UK	balhammoud@argans.co.uk
Prepared by	J. Hedley	Numerical Optics Ltd, UK	j.d.hedley@envirocs.com
Reviewed by	J. Hedley Marc Bouvet	NOL ESTEC	j.d.hedley@envirocs.com Marc.Bouvet@esa.int
Approved by	Marc Bovet	ESTEC	Marc.Bouvet@esa.int

Acknowledgements

Version History

Version	Date	Main Changes
1.0	28/05/2014	ATBD ref: 003-013: MO-SCI-ARG-TN-004b Edited to reflect the implementation in DIMITRI V3.0 onward
2.0	28/03/2019	The ATBD is updated to reflect the implementation in DIMITRI V4.3.1 onward. Mainly the implementation of the Hyperspectral LUTs "Ref: ARG_DIM_QA4EO_LUT_SUM" Including the Water leaving BRDF "Ref: ARG_DIM_QA4EO_WL_BRDF" And Atmospheric pressure adjustment "Ref: ARG_DIM_QA4EO_ATM"
2.1	26/09/2019	Overall the ATBD revision and added reference (Bouvet 2013)

TABLE OF CONTENTS

List of Figures

List of Tables

1   Introduction

1.1   Scope of this ATBD

Under ESA contract 4000114544/15/I-SBo ("QA4EO-DIMITRI Evolution") DIMITRI v3.x.y has been merged with DIMITRI v4.2.4 and further developed into DIMITRI v4.x.y (v4.3.1 onward), in which both the Rayleigh scattering and Sun-glint interband calibration methodologies originally developed by ARGANS have been improved. The two corresponding ATBDs are:

Absolute vicarious calibration over Rayleigh Scattering

Interband vicarious calibration over Sunglint

This ATBD document describes the methodology for the Absolute calibration over Rayleigh Scattering over ocean. The document is organized as follow:

1) Introduction to the ATBD
2) Describes the principles of this method;
3) Sensitivity analyses and uncertainty estimations;
4) Presentation of the implementation in DIMITRI v4.x making use of Hyperspectral LibradTran LUTs and Hydrolight version 5.2 model (Mobley and Sundman 2013);
5) The results of the implementation, sensitivity analyses and uncertainty estimations;

1.2   DIMITRI

The Database for Imaging Multi-Spectral Instruments and Tools for Radiometric Intercomparison (DIMITRI) is an open-source software offering users the capability of radiometric performance assessment of optical imagers. It is coupled to a database of L1b products from a number of optical medium resolution sensors.

DIMITRI offers a suite of tools for comparison of the L1b radiance and reflectance values originating from various medium resolution sensors over a number of radiometrically homogenous and stable sites (Table 1) at TOA level, within the 400nm – 4μm wavelength range. The database (available separately from the software) covers the period 2002 to present. DIMITRI's interface enables radiometric intercomparisons between sensors or against simulated signals (over ocean and desert sites).

After extraction from L1b products, the DIMITRI database contains for each site the mean reflectance and standard deviation (and number of valid pixels in the defined region of interest, or ROI), the viewing and solar geometries and auxiliary and meteorology information where available (windspeed and direction, surface pressure, humidity and ozone concentration). Each observation is automatically assessed for cloud cover using automated algorithms making use of

each sensors spectral coverage; manual cloud screening can also be visually performed using product quicklooks to flag misclassified observations. Other capabilities and functions include: product reader and data extraction routines, database status visualisation and instrument spectral response comparison tool.

DIMITRI v2.0 offered two methodologies for radiometric performance assessment:

1. **Radiometric intercomparison based on angular and temporal matching**, based on the methodology of Bouvet (2006) and Bouvet *et al* (2007): Concomitant observations made under similar geometry and within a defined temporal window are intercompared at similar spectral bands.

2. **Radiometric intercomparison of VEGETATION simulated and actual observations**, making use of the ability to combine timeseries from all sensors into one "super sensor" and fitting a 3-parameter BRDF model to all observations to simulate TOA spectra of VEGETATION-2 (Bouvet, 2011).

DIMITRI v3.x is evolved from DIMITRI v2.0 and has two additional methodologies (below) and an improved automated cloud screening and cloud screening tool. Moreover the second methodology if DIMITRI v2.0 above was replaced by the methodology described in (Bouvet 2014) allowing simulating the TOA signal over desert sites.

In parallel to DIMITRI v3.x development, a new version v4.0 was developed by MAGELLIUM including new radiometric comparison methodologies (over ocean and desert sites) and aiming at giving a sounder software basis (improving modularity). **DIMITRI v4.3.1** is evolved from the merging of DIMITRI v3.x.y and DIMITRI v4.0. Furthermore , two methodologies originally present in DIMITRI v3.x were improved:

1. **Absolute vicarious calibration over Rayleigh Scattering,** based on the methodology of Hagolle *et al* (1999) and Vermote *et al* (1992) and utilising open ocean observations, to simulate molecular scattering (Rayleigh) in the visible and comparing against *the observed* ρ_{toa} to derive a calibration gain coefficient;

2. **Vicarious calibration over sunglint**, based on the methodology of Hagolle *et al* (2004); similar to Rayleigh scattering approach but accounting for sunglint reflectance contribution;
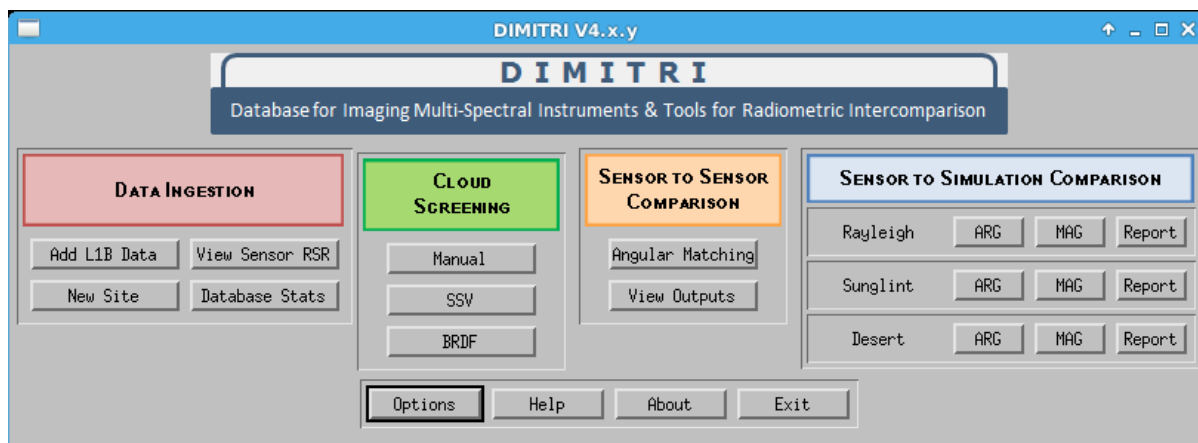
Figure 1: DIMITRI v4.x.y screenshot

Table 1: Sensors and sites included in the DIMITRI v4.x.y database

Sensor	Data Supplier
AATSR	http://ats-merci-ds.eo.esa.int/merci/welcome.do
ATSR2	http://ats-merci-ds.eo.esa.int/merci/welcome.do
Landsat-8/OLI	https://landsat.usgs.gov/landsat-data-access
MERIS	http://merci-srv.eo.esa.int/merci/welcome.do http://www.odesa-info.eu/
MODIS-Aqua	http://ladsweb.nascom.nasa.gov/
PARASOL	http://polder.cnes.fr/en/index.htm
VEGETATION – 2*	http://www.vito-eodata.be
VIIRS	http://ladsweb.nascom.nasa.gov/

Sensor	Data Supplier
Sentinel-2A/MSI	
Sentinel-2B/MSI	
Sentinel-3A/OLCI	https://scihub.copernicus.eu/
Sentinel-3B/OLCI	
Sentinel-3A/SLSTR	
Sentinel-3B/SLSTR	

Site name	Site Type	North Latitude	South Latitude	East Longitude	West Longitude
AMAZON	Forest	1.33	1	-56.5	-57
DOME C	Ice	-74.9	-75.3	123.9	122.9
UYUNI	Salt	-20	-20.16	-67.45	-68.05
TUZ GOLU	Salt	38.8	38.7	33.4	33.25
ALGERIA-3	Desert	30.82	29.82	8.16	7.16
ALGERIA-5	Desert	31.52	30.52	2.73	1.73
LIBYA-1	Desert	24.92	23.92	13.85	12.85
LIBYA-4	Desert	29.05	28.05	23.89	22.89
MAURITANIA-1	Desert	19.9	18.9	-8.8	-9.8
MAURITANIA-2	Desert	21.35	20.35	-8.28	-9.28
BOUSSOLE	Ocean	43.45	43.25	8	7.8
SIO	Ocean	-30	-30.5	80.5	80
SPG	Ocean	-31	-31.5	-137	-137.5
SPG_OPTIMUM	Ocean	-24	-28	-118	-122
SIO_OPTIMUM	Ocean	-25	-29	80	76
NW_PACIFIC_OPTIMUM	Ocean	20	16	159	155
NE_PACIFIC_OPTIMUM	Ocean	20	16	-150	-154
NW_ATLANTIC_OPTIMUM	Ocean	25	21	-65	-69

SW_ATLANTIC_OPTIMUM	Ocean	-12	-16	-22	-26
MEDSEA_OPTIMUM	Ocean	34	33	33	32
NE_AUSTRALIA_OPTIMUM	Ocean	-18	-20	155	153

DIMITRI_v2.0 and v3.0 are freely available (without the L1b database). DIMITRI_v2.0 is available following registration at www.argans.co.uk/dimitri. DIMITRI_v3.0 is a larger file (approx. 55GB) so is available upon request; ARGANS or ESA will make it available on an FTP server site.

DIMITRI_v4.x.y is still under development and validation, and will be released when fully validated.

2 Rayleigh Scattering Absolute Calibration

2.1 Overview

Rayleigh calibration methodologies utilise open ocean observations with low aerosol content, in which the main component of the TOA signal in the visible wavelengths is the molecular scattering (Rayleigh); this scattering by molecules is well characterised and can be accurately computed. Other contributing components to the TOA signal include scattering by aerosols, the marine reflectance, specular reflection of the water surface (known as Fresnel reflectance), sun glint, gaseous absorption (e.g. ozone, water vapour, trace gases etc) and reflection from whitecaps. In these regions the TOA signal can be simulated using an analytical TOA reflectance model and a set of LUTs resulting from radiative transfer simulations carried out with the libradtran package.

Absolute calibration methodologies such as Vermote *et al* (1992) and Hagolle *et al* (1999) aim to measure an absolute calibration coefficient, A^k. The Hagolle *et al* (1999) approach is implemented in DIMITRI. This method, which builds on the Vermote *et al* (1992) approach, uses careful pixel selection to remove the contribution from white caps and sun glint through the selection of low wind speeds and pixels outside of the specular reflection geometry. Open ocean regions far away from dynamic coastal processes have been shown to have relatively stable marine reflectances (Fougnie *et al*., 2002); climatological chlorophyll concentrations are used to estimate the marine reflectance using established surface reflectance models such as Morel (1998).

Following the detailed pixel criteria selection Vermote *et al* (1992) and Hagolle *et al* (1999) define the calibration coefficient A^k, computed using different aerosol models and chl-a concentrations, and then averaged over the sensor time series to provide one single calibration coefficient, for example as shown in Figure 2.

The Rayleigh contribution to the TOA signal, although large in the blue wavelengths, decreases considerably towards the Near Infrared (NIR); at these wavelengths the main contribution comes from the aerosol scattering (zero marine reflectance) and this can be used to provide an estimate of the aerosol properties. Using pre-defined aerosol models (Shettle and Fenn, 1979), the aerosol contribution in the NIR can be used to estimate the contribution in the visible wavelengths and thus allow simulation of the TOA reflectance. The Rayleigh method thus compares the model predicted reflectance to the observed reflectance to derive an estimation of the absolute calibration coefficient. This method cannot be applied to wavelengths above 700 nm since the Rayleigh scattering radiance becomes too small in the near infrared.

Figure 2: POLDER in-flight Rayleigh calibration coefficients from 100 orbits using the M98 Aerosol Model and a chl-a concentration of 0.035 mg.m^{-3}. From Hagolle *et al* (1999)

Calibration targets are selected in order to minimise the non-molecular radiance sources: a clear atmosphere is necessary, above a dark target (ocean, with a low wind speed to avoid whitecaps). The main error sources for this calibration method are the water reflectance estimation and the aerosol optical thickness estimation. In order to better define the water body contribution, the method is applied to oceanic zones where the chlorophyll concentration is stable. The aerosols are the most variable part of the atmospheric radiance and could induce errors in the absolute calibration. Very clear atmospheres are thus selected using a threshold on the reflectance measured in a near infrared band (around 850 nm). Besides, for the selected pixels, the 865 nm reflectance is used to determine the expected aerosol reflectance in the calibrated band (Green and Chrien, 1999). For this extrapolation, it is necessary to rely on an aerosol type. The M98 (Maritime model with 98% of humidity) is generally used as the most likely. The Rayleigh based method is generally applied for large Field of View sensors. In this case, the method is applied as described in the paragraph above and the outputs are averaged on a significant number of images. The Rayleigh method can also be applied to small FOV sensors. It is mostly land sensors that occasionally acquire, on purpose, images over the open ocean. One way to get information on the aerosol model as well on the water contribution is to use simultaneous images of "ocean colour" sensors which provide at level 2 the relevant information: aerosol model and chlorophyll a amount.

Fougnie and Henry (2009) justify usage of Rayleigh scattering as the basis for calibration by the fact that molecular scattering may constitute as much as 90% of the TOA signal, for blue to red spectral bands. Climatology is used for marine reflectance, and cases too contaminated by aerosols are rejected, in contrast with vicarious radiometric calibrations using in-situ measurements in which the TOA signal is accurately computed using measurements of aerosol optical properties and water-leaving radiance. The advantage of the method using Rayleigh scattering is that the calibration is neither geographically nor geophysically limited, but is derived from a large set of oceanic sites, from both hemispheres and for a large set of conditions.

Hagolle *et al* (1999) comment that this methodology is an efficient method for absolute calibration of optical instruments without the need for in-situ measurements.

The method provides calibration coefficients with a 3-4% uncertainty for spectral bands 490 nm and 565 nm. Hagolle *et al* (1999) point out that the use of oligotrophic waters is not the ideal case for the calibration of 443 channel due to high water-leaving radiances, and yet, it is not easy to find ocean zones away from the coasts with high and stable chlorophyll concentrations.

The use of in-situ measurements can therefore enhance results; Fougnie *et al*. (1999) have acquired in-situ data of water-leaving radiances, using SIMBADA instruments quasi-simultaneously with POLDER acquisitions.

2.2 Algorithm Description

A Rayleigh Scattering calibration methodology has been developed based on Vermote *et al*. (1992) and Hagolle *et al*. (1999) and is applicable to any optical sensor that acquires images over predefined sites (see Table 1). The following sections summarises the dataset, signal modelling and vicarious coefficient computation.

2.2.1 Oceanic sites

Rayleigh calibration is applicable on stable oceanic regions, with low concentration of phytoplankton and sediment in order to neglect the marine signal at 865 nm, and far from land to ensure a purely maritime aerosol model. Several regions in DIMITRI are good candidates (Table 1).

2.2.2 Data screening

Clear conditions must be chosen to avoid any signal contamination by clouds, haze or cloud shadows. As we shall see, a 0% cloud coverage at ROI level is mandatory for proper computation of the vicarious coefficients.

A low wind speed is required for ensuring no presence of whitecaps; typically it is limited to 5 m/s.

Small content of aerosol must be insured for avoiding any error propagation in the atmospheric path radiance. We follow Hagolle *et al*. (1999) by considering the Rayleigh corrected normalised radiance at 865 nm (directly related to aerosol amount):

$$R_{RC}(865) = (\rho_{TOA}(865) - \rho_R(865)) \cos \theta_s \qquad (1)$$

The very stringent threshold at 865 nm of 0.002 also avoids using further data screening for sun

glint.

2.2.3   Marine model

In DIMITRI versions prior to V4.3.1, the marine model follows Morel and Maritorena (2001), which is an update of Morel (1988) used in Hagolle *et al*. (1999). It provides an estimate of irradiance reflectance at null depth, R(0⁻) , from 350 to 700 nm, as a function of chlorophyll concentration and sun zenith angle, but it does not take in account for the viewing geometry (c.f. neglecting the BRDF effects).

The simplest method to incorporate BRDF effects in L_w is to replace $\rho_w(\lambda)$ with a directionally dependent value $\rho_w(\lambda, \theta_s, \theta_v, \Delta\phi)$. Therefore implementing the water leaving BRDF in terms of $\rho_w(\lambda, \theta_s, \theta_v, \Delta\phi)$ will lead to a potential overestimate of the BRDF effect at TOA, because the assumption is that the total transmission is entirely direct transmission. In reality, atmospheric scattering redistributes a portion of the light and will 'blur out' the BRDF effect. Previous investigation has indicated that the libRadtran Mystic solver lacks the capability for directionally tabulating the radiance at BOA, as would be required to do this (Hedley 2017). Since the reflectance is dependent on the chlorophyll concentration, the actual requirement is for a five parameter function, $\rho_w(\lambda, \theta_s, \theta_v, \Delta\phi, [chl])$, where [chl] is the chlorophyll concentration in mg m⁻³. For the implementation in DIMITRI, this function has been tabulated as a five dimensional look-up table (LUT), more details in (Hedley 2017).

Since HydroLight is now used to generate the BRDF LUT, where it calculates by exact physical methods based on the water absorption and volume scattering function, and provides water leaving radiance (L_w) directly, as did the Monte Carlo model used by Morel and Gentili.

The basis of the current DIMITRI water leaving reflectance model lies in Morel (1988) where it is stated by reference to work by Gordon and Kirk that subsurface irradiance reflectance, $R(0-)$ is to a good approximation expressed by:

$$R = 0.33\frac{b_b}{a}$$

(2)

At that time is was suggested that the factor 0.33, which later became denoted f, varied only slightly due to illumination conditions, supported by the paper of Kirk (1981). The paper on which the current DIMITRI reflectance model is based (Morel and Maritorena 2001) is concerned primarily with b_b/a component of this expression and says relatively little about f, which in DIMITRI is fixed at 0.33 as above.

In order to translate subsurface irradiance reflectance $R(0-)$ to above surface reflectance

additional terms are required, and this results in the expression as appears in the DIMITRI Rayleigh calibration ATBD

$$\rho_w(\lambda) = \pi \frac{\Re}{Q} R(0^-) \qquad (3)$$

Where:

$\Re$ is the term accounting for all the reflection and refraction effects, with averaged value of 0.5287 for moderate wind speed (see Appendix D of Morel and Gentili, 1996); and

Q which can be interpreted as the ratio of the upwelling radiance to the upward planar irradiance just below the surface, i.e. $Q = L_u(0^-) / E_u(0^-)$. Q is a measure of the anisotropy of the upwelling radiance below the surface, in DIMITRI it is fixed as π which implies isotropic upwelling radiance (radiance equal in all directions over the upward hemisphere). The satellite sensor of course does not see the result of the irradiance reflectance of the surface, it primarily sees the radiance reflected in a particular direction. So although the application of π in a sense implies isotropic upward radiance above the surface this π term isn't relevant as part of the BRDF.

Combining equations 2 and 3 above leads to the expression presented in Morel and Gentili (1996), which is the full expression of what is required for DIMITRI in the terms of the parameters discussed:

$$L_w(\theta, \theta_0, \Delta\phi) = E_d(0^+)\Re(\theta) \frac{f}{Q} \frac{b_b}{a} \qquad (4)$$

Multiplying the output of this equation (L_w) by π gives ρ_w. The terms f and Q are dependent on solar-view geometry although this dependence is not shown above. In Morel and Gentili (1996) f is considered primarily dependent solar zenith, θ_s, while Q is potentially dependent on the full solar-view geometry expressed by θ_s, θ_v and $\Delta\phi$. The key point is that the BRDF properties are entirely captured by $\Re \times f/Q$, and for θ_v less than 60° primarily by f/Q because $\Re$ is almost constant. While f and Q individually vary with solar zenith angle to quite a large degree, their individual variations cancel out to some extent so that the overall effect on water leaving BRDF is reduced (Figure 3)

	DIMITRI_v4.x ATBD Rayleigh Scattering Methodology for Vicarious Calibration	**Reference:** ARG_DIM_QA4EO - TN-004b **Revision:** 2.1 **Date:** 26/09/2019 **Page:** 11

ARGANS
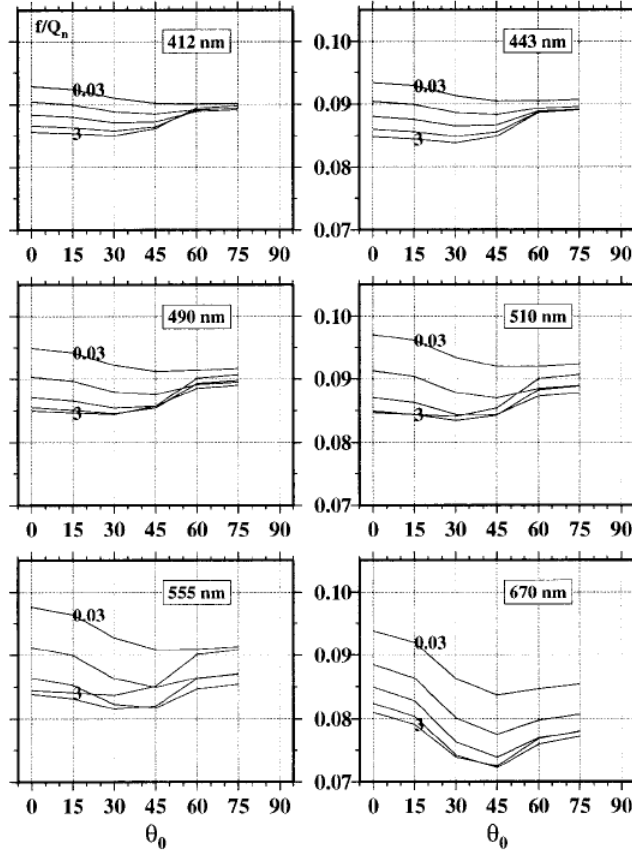
Figure 3: Variation in f/Q with solar zenith angle (here θ_0) and chlorophyll concentration (0.03 to 3 mg m^{-3}). Reproduced from Moral and Gentili (1996).

In order to replicate the water leaving BRDF presented by Moral and Gentili (1996) and tabulate it in a form that can be used in DIMITRI, the software HydroLight version 5.2 has been used (Mobley and Sundman 2013).

The model provides close agreement to both the current DIMITRI reflectance function, based on Morel and Maritorena (2001), and the BRDF effects shown in Morel and Gentili (1996) (Figure 4). The final structure of the LUT is given in (Table 7; see Hedley 2017). Note the tabulated values are $L_w/E_d(0+)$ so must be multiplied by π to give ρ_w.

The comparison between HydroLight and Morel and Gentili f/Q results (Figure 5) is good for θ_v less than 60°. Note Figure 5 is presented in terms of the sub-surface refracted solar zenith angle θ', so $\theta' = 40°$ is $\theta_v \approx 60°$. Recalling that f/Q encapsulates the BRDF effect, Figure 5 shows that

the HydroLight BRDF is in generally good agreement with the results of Morel and Gentili. The difference seen in Figure 5 at view angles greater than 60° is due to taking a fixed value of $\Re$. The HydroLight results contain the 'true' view-dependent $\Re$ and are correct.
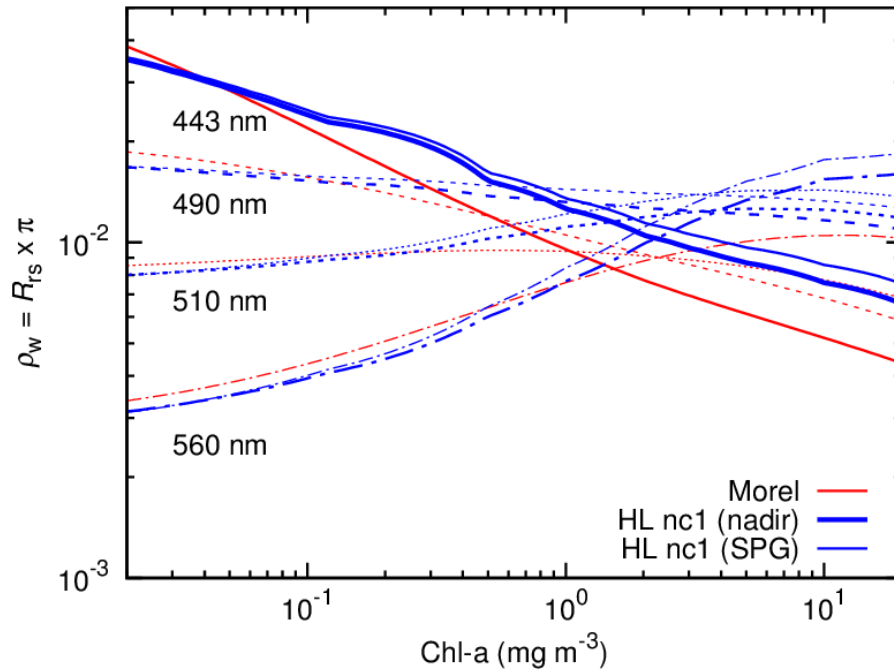
Figure 4: Comparison of the Morel and Maritorena (2001) reflectance model with Hydrolight New Case 1 model at a nadir solar-view geometry, $\theta_s = 0$, $\theta_v = 0$, and also a typical SPG solar-view geometry, $\theta_s = 50°$, $\theta_v = 20°$ and $\Delta\phi = 60°$, with wind speed $u_{10} = 0.5$ ms^{-1}. Four wavelengths are shown, as labelled. The Morel and Maritorena is applied as implemented in DIMITRI, with f = 0.33 and Q = π i.e. f/Q = 0.105.
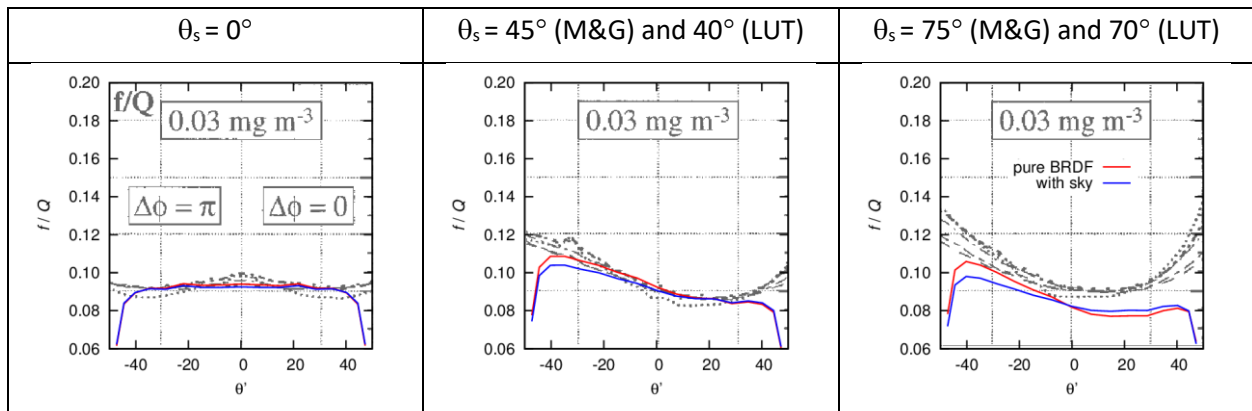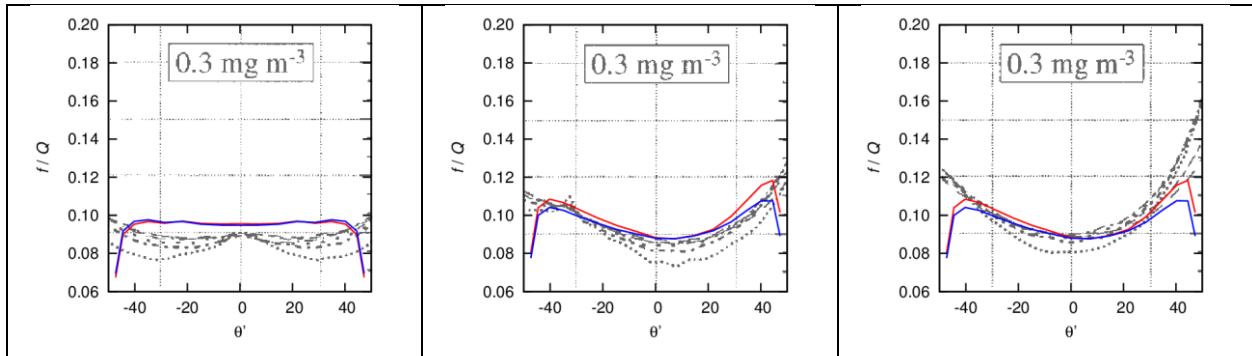
Figure 5: Comparison of f/Q from Morel and Gentili (1996) and the BRDF produced with the HydroLight New Case 1 model. HydroLight results at 440 nm are the blue and red lines, the Morel and Gentili results represent several wavelengths with 440 nm generally being one of the upper lines. Red lines are 'pure BRDF' values assuming light is incident from the solar direction only. Blue lines include the HydroLight sky radiance model for typical clear sky conditions.

2.2.4   Atmospheric model

The total TOA signal can be written as:

$$\rho_{TOA}(\lambda) = t_{gas}(\lambda)\big(\rho_{path}(\lambda) + t_{down}(\lambda) * t_{up}(\lambda) * \rho_w(\lambda) + T_{down}(\lambda) * T_{up}(\lambda)\rho_G\big) \quad (5)$$

Where:

t_{gas} is the transmittance (downward and upward) due to absorbing gas as O3, O2 and H2O

ρ_{path} is the atmospheric reflectance due to Rayleigh and aerosols and their multiple-scattering interaction

t_{down} and t_{up} are respectively the downward and upward total transmittance (i.e. direct + diffuse) due to Rayleigh and aerosol

ρ_w is the marine signal already described

T_{down} and T_{up} are the downward and upward direct transmittances

ρ_G is the sun glint reflectance at sea level.

Data selection in the Rayleigh calibration is such that:

- ρ_G is neglected
- ρ_w is neglected in the near-infrared (band 865 nm especially)

Rayleigh calibration coefficients are computed for all DIMITRI bands in the visible domain; we extend the original limit at 550 nm of Hagolle *et al*. (1999) up to 670 nm, as done more recently by Fougnie *et al*. (2012). Also the near-infrared 865 m band is used to estimate aerosol optical thickness (see next section). The methodology must not be applied to sensors having spectral bands in which there is significant water vapour absorption. For instance, for MERIS the only atmospheric gas impacting these bands is ozone, if we neglect residual water vapour absorption at 665 and 865 nm, as done for instance in the operational MERIS processing (MERIS DPM, 2011). Hence the gaseous transmittance is computed by Beer's law:

$$t_{gas}(\lambda) = t_{O_3}(\lambda) = e^{-\tau_{O_3}(\lambda)*O_3*M} \tag{6}$$

Where:

O_3 is the ozone concentration of actual measurement

τ_{O_3} the ozone optical thickness at a standard concentration (already provided in DIMITRI auxiliary data)
M the air mass fraction.

The path reflectance and total transmittance are computed by radiative transfer simulations (see hereafter) for a set of aerosol models and optical thicknesses, and stored in Look-up tables (LUT). Aerosols models must be representative of the calibration zone; marine models of Shettle and Fenn (1974) are here chosen for several relative humidity. Other more complex models may also be used for sensitivity study.

The aerosol optical thickness retrieved from a direct LUTs interpolation. Note that the AOT LUT is the result of direct calculation from the aerosol model and does not contain Monte Carlo noise unlike the other LUTs (see Hedley 2018 ATBD-LUTs-SUM).

$$\tau_a(\lambda) \rightarrow LUTs\ Linear\_interpolation\left(\lambda, w_m, \theta_s, \theta_v, \Delta\varphi\right) \tag{7}$$

Radiative transfer simulations are only tabulated for the unique standard atmospheric pressure. Because the actual measurements are under different pressures, P, generally systematically higher due to clear sky condition, a correction on ρ_{path} and $t_{down} * t_{up}$ and $T_{down} * T_{up}$ are necessary and done following (Bodhaine et al. 1999; Hedley 2018 ATBD-Pressure correction).

The pressure correction algorithm makes direct use of the hyperspectral HS147 LUTs for atmospheric reflectance (ρ_{path}) and for upward and downward transmission (t_u and t_d).
In the pressure correction it is assumed that the wavelength at the band centres is representative of the full band width, this is necessary because it is not feasible to pre-calculate corrections

resampled to the band RSRs. Any error is likely to be negligible for narrow bands such as MERIS or OLCI, and for wider bands, such as Sentinel 2, the issue of neglecting within-band spectral calculations is a limitation for in DIMITRI in general. In the reference code (see below) all calculations are performed hyperspectrally and convolved to band RSRs at the end.

1. Initialisation

Construct a table of wavelength, λ, and Rayleigh optical thickness, τ_r, according to standard LUT. i.e. columns 1 and 2 from Hedley 2018 ATBD-Pressure correction. The purpose of this table is to allow an interpolated log-log look-up to give wavelength as a function of Rayleigh optical thickness (Figure 6) therefore it may be most efficient to tabulate the natural log of λ and τ_r.
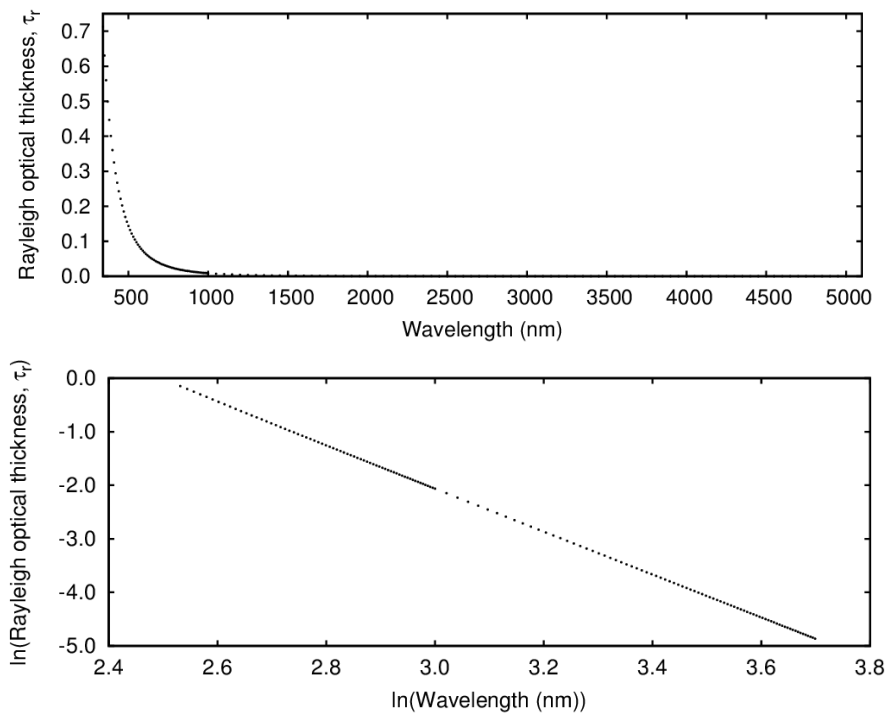
Figure 6: Effect of wavelength on Rayleigh optical thickness as direct values (top), and log-log values (bottom). Calculated according to Bodhaine et al. (1999) and method described in Section 3.

Then for each image subset to be processed:

2. Correction of ρ_{path}

At any point at which the band ρ_{path}(band) is read from the RSR resampled LUT:

2.1 Read the corresponding $\rho_r(\lambda)$ from the hyperspectral LUT, that is according to the same solar-view geometry and wind speed. Where λ is the band centre and $\rho_r(\lambda)$ is value obtained when the aerosol optical thickness τ(550) is set to zero.

2.2 Calculate the Rayleigh optical thickness, τ_r, for the pressure, latitude and CO_2 corresponding to the image subset following Bodhaine et al. 1999 (detailed in Hedley 2018 ATBD).

2.3 Find by log-log interpolation of the table prepared in the initialisation (Figure 6) the wavelength at which this τ_r occurs, denoted λ_{adj}.

2.4 Read $\rho_{path}(\lambda_{adj})$ and $\rho_r(\lambda_{adj})$ from the hyperspectral LUT.

2.5 Correct ρ_{path}(band) by applying the following calculation, which applies the change in Rayleigh reflectance between the standard wavelength, λ, and the wavelength that has the desired Rayleigh optical thickness, λ_{adj}.

$$\rho_{path}(\lambda) \rightarrow \rho_{path}(\lambda) + \rho_r(\lambda_{adj}) - \rho_r(\lambda) \qquad (8)$$

3. Correction of total transmission $t_u \times t_d$

The band transmissions t_u(band) and t_d(band) must similarly be corrected for the change in Rayleigh optical thickness, in practice these are used only as their product, total transmission t_u(band) $\times t_d$(band), and are read from the RSR resampled LUTs at the same time as ρ_{path}(band). Steps 2.2 and 2.3 above, estimation of λ_{adj}, are common with the ρ_{path} correction, so at any point after step 2.3 do this:

3.1 Read the corresponding $t_{ur}(\lambda)$ and $t_{dr}(\lambda)$ from the hyperspectral LUT, as a function of solar-view geometry. Where λ is the band centre and $t_{ur}(\lambda)$ and $t_{dr}(\lambda)$ are the values obtained when the aerosol optical thickness τ(550) is set to zero.

3.2 Read $t_{ur}(\lambda_{adj})$ and $t_{dr}(\lambda_{adj})$ from the hyperspectral LUT.

3.3 Correct t_u(band) $\times t_d$(band) by applying the following calculation, which applies the change in transmission between the standard wavelength, λ, and the wavelength that has the desired Rayleigh optical thickness, λ_{adj}. Note the effect here is assumed multiplicative, whereas for ρ_{path} it was considered additive.

DIMITRI_v4.x ATBD
Rayleigh Scattering Methodology for Vicarious Calibration

Reference: ARG_DIM_QA4EO - TN-004b
Revision: 2.1
Date: 26/09/2019
Page: 17

$$t_u(\lambda) \times t_d(\lambda) \rightarrow [t_u(\lambda) \times t_d(\lambda)] \times [t_{ur}(\lambda_{adj}) \times t_{dr}(\lambda_{adj})] / [t_{ur}(\lambda) \times t_{dr}(\lambda)] \quad (9)$$

4. Correction of total transmission $T_u \times T_d$

Where direct transmission occurs it can be corrected by noting that the component of the direct transmission due to Rayleigh scattering is proportional to Rayleigh optical thickness and fully decoupled from the aerosol contribution. Direct transmission is losses to a beam which occur after a single scattering event. Direct transmission due to Rayleigh in the upward or downward path is

$$T(\lambda) = \exp[-M \times \tau_r(\lambda)] \quad (10)$$

where M is the air mass, i.e. relative path length, for the upward or downward path, $M = 1 / \cos\theta$.

The correction for T_u(band) and T_d(band) is performed by dividing through by the transmission due to Rayleigh optical thickness at the band centre (removing the 'standard' Rayleigh transmission) and then multiplying by the transmission with the desired Rayleigh optical thickness $\tau_r(\lambda_{adj})$. For downward transmission:

$$T_d(\lambda) \rightarrow T_d(\lambda) \times \exp[M_d \times \tau_r(\lambda) - M_d \times \tau_r(\lambda_{adj})] \quad (11)$$

For the upward transmission the expression is the same, but replacing M_d with the upward path length M_u. The correction relies only on the tabulated reference Rayleigh thicknesses (Figure 6) and the Rayleigh thickness function (See above). Note that the hyperspectral LUTs are not used in the direct transmission correction.

5. Aerosol optical thickness determination

The aerosol optical thickness determination is performed by an interpolation of the look-up on the band LUT ρ_{path}(band) values at the reference band (e.g. 865 nm). Pressure correction therefore simply requires each of those values to be corrected as described above before the interpolated look-up. The total transmission correction is not required in the aerosol thickness determination.

2.2.5 Calibration coefficient algorithm

The algorithm consists of following steps, repeated for all bands λ:

1. Given an aerosol model chosen by the user (currently MAR99 only), retrieve the aerosol optical thickness at 865 nm by an interpolation of the look-up table (see above).

   1.1. Compute Rayleigh optical thickness and Rayleigh reflectance at 865 nm
   1.2. Correct $\rho_{TOA}(865)$ at standard pressure following Bodhaine 99 (see above).

$$\rho_{TOA}(865)_{|P_{std}} \rightarrow \rho_{TOA}(865) + \rho_r(\lambda_{adj}) - \rho_r(\lambda) \tag{12}$$

   1.3. Inverse optical thickness Look-up (linear inversion)

$$\tau_{865} \xleftarrow{LUT\ aer} \rho_{TOA}(865)_{|P_{std}} \tag{13}$$

2. Propagate aerosol optical thickness through tabulated spectral dependence:

$$\tau_{865} \xrightarrow{LUT\ aer} \tau_\lambda = \tau_{865} * c_\lambda \tag{14}$$

3. Compute total path radiance (Rayleigh + aerosol) and correct for pressure:

$$\tau_\lambda \xrightarrow{LUT\ aer} \rho_{path}(\lambda)_{|P_{std}} = \rho_{path}(\lambda, \tau_\lambda, w_m, \theta_s, \theta_v, \Delta\varphi) \tag{15}$$

$$\rho_{path}(\lambda)_{|P} = \rho_{path}(\lambda)_{|P_{std}} + \rho_r(\lambda_{adj}) - \rho_r(\lambda) \tag{16}$$

4. Compute downward and upward total transmittances (direct + diffuse), accounting for Rayleigh and aerosol, and correct for pressure:

$$\tau_\lambda \xrightarrow{LUT\ aer} t_{dn}(\lambda)_{|P_{std}} = \{t_{dn}\}(\lambda, \tau_\lambda, w_m, \theta_s) \tag{17}$$

$$\tau_\lambda \xrightarrow{LUT\ aer} t_{up}(\lambda)_{|P_{std}} = \{t_{up}\}(\lambda, \tau_\lambda, \theta_v) \tag{18}$$

$$t_{dn}(\lambda) * t_{up}(\lambda)_{|P} = t_{dn}(\lambda) * t_{up}(\lambda)_{|P_{std}} * [t_{ur}(\lambda_{adj}) * t_{dr}(\lambda_{adj})] / [t_{ur}(\lambda) * t_{dr}(\lambda)] \tag{19}$$

5. Given a chlorophyll concentration and solar-view geometry, compute marine reflectance at band λ_{ref} from Look-up tables using HydroLight version 5.2 model (Mobley and Sundman 2013)

$$\pi \times \text{linear interpolated lookup } (\lambda, \theta_s, \theta_v, \Delta\phi, [\text{chl}]) \rightarrow \rho_w(\lambda_{ref}) \tag{20}$$

6. Construct theoretical TOA signal by:

$$\rho_{TOA}^{theo}(\lambda) = \rho_{path}(\lambda)_{|P} + t_{dn}(\lambda) * t_{up}(\lambda)_{|P} * \rho_w(\lambda) \tag{21}$$

7. Correct the measured TOA signal for ozone:

$$\rho_{TOA}^{oz}(\lambda) = \rho_{TOA}(\lambda)/t_{O_3}\lambda \tag{22}$$

8. Eventually compute the Rayleigh calibration coefficient (relative to L1b calibration) by:

$$RA(\lambda) = \frac{\rho_{TOA}^{oz}(\lambda)}{\rho_{TOA}^{theo}(\lambda)} \tag{23}$$

It is worth highlighting the main differences with this method compared to the Hagolle *et al.* (1999) method:

- The marine model is updated from Morel (1988) to Morel and Maritorena (2001);
- The aerosol optical thickness is retrieved at 865 nm by inversion of LUTs using segment-wise linear=interpolation on band ;
- Propagation of the path atmospheric signal from 865 nm to the visible is made directly using the RTM simulations as a function of optical thickness;
- Downward and upward transmittances include the aerosol contribution.
- The pressure correction is applied following Bodhaine et al. 1999.

- The computing of Water Leaving reflectance takes in account the directional effects of BRDF.

.

DIMITRI_v4.x ATBD
Rayleigh Scattering Methodology for Vicarious Calibration

Reference: ARG_DIM_QA4EO - TN-004b
Revision: 2.1
Date: 26/09/2019
Page: 21

3 Uncertainty analysis

3.1.1 Published error budget

According to Hagolle *et al* (1999), the following are the main error sources for the methodology:

- Ozone amount (less than 0.5% uncertainty on the calibration at 490 and 443 nm)
- Wind speed: this modifies the sunglint geometry
- Surface pressure: accurately known, it leads to 0.1% on the 3 POLDER channels
- Aerosol amounts: the 865 nm channel is used to discard turbid atmospheres or to estimate aerosol contribution on clear ones. Simulations show that the impact of aerosol model on calibration coefficients is always under 1%. Calibration errors in the 865 nm band also result in some errors in the aerosol correction (5% for 865 nm calibration induces 1% error on 565 and less for 443 and 490 nm).
- The water-leaving radiance is the main uncertainty for the 443 nm channel. An error of 50% on Chlorophyll concentration leads to an uncertainty on calibration coefficient up to 2% for a 443 nm channel.

This leads to a total published uncertainty of 4% maximum. It is worth noting this uncertainty is relatively large considering that calibration coefficients are in practice of around few percent around unity.

3.1.2 Sensitivity analysis on DIMITRI data

The main sources of uncertainty of the vicarious calibration are:

- The input parameters listed above;
- The data screening condition, i.e. mainly clouds;
- The pixel averaged on the calibration region.

Therefore a sensitivity analysis can be conducted with DIMITRI implementation to update the previously mentioned total error budget and to add new terms. We do not recompute uncertainty due to ozone, wind speed and pressure as radiative transfer modellings are analogous between Hagolle *et al* (1999) and DIMITRI. Let us note that the published 0.1% uncertainty due to pressure is in line with our previous analysis, showing that 1.5hPa error lead to 1.5/1013.25*0.7=0.1% error on the calibration coefficient at 412 nm, and less towards the red channels. In the following, the nominal run is a calibration of MERIS over SPG, with default options, in particular a MAR-99 aerosol model.

Sensitivity to clouds coverage: accepting 10% cloud coverage at ROI level, without considering pixel-by-pixel cloud mask, increases the number of calibration points from 19 to 44 and changes

the median vicarious coefficients from less than 4% at 412 nm to less than 1% at 665 nm; standard deviation of individual coefficients is unchanged. This shows that the threshold at 865 nm is not enough to discard cloudy pixels yet well identified by the cloud screening, or possibly their shadows. In conclusion the 0% cloud coverage option at ROI level should be kept for providing less than 5% uncertainty in the blue bands (taking into account other sources of uncertainty), when the pixel-by-pixel cloud mask information is not used.

Sensitivity to aerosol model: switching to model MAR-70 or COAST-70 lead to less than 0.8% error at all bands, slightly higher than in Hagolle *et al*. (1999).

Sensitivity to chlorophyll: replacing the chlorophyll monthly climatology by its extreme values (0.04 and 0.08 mg/m^3 over SPG) impacts on average the coefficients from 3% at 412 nm to 0.15% at 665 nm. We thus retrieve the conclusion of Hagolle *et al*. (1999), that the main driver of Rayleigh vicarious calibration is the chlorophyll concentration, in particular in the blue wavelengths.

Sensitivity to sensor noise (pixel averaging): this can be assessed by comparing the DIMITRI output coefficient starting either from the averaged TOA signal, or from the pixel-by-pixel extraction (see section 3.3.3 about this processing mode). A first effect of using the averaged mode is to decrease even more the number of calibration points (from 19 to 9), while not improving the calibration coefficient dispersion. The impact is of about 1.3% at 412 nm and less than 1% at other bands.

The total error budget is about 5.9% at 412 nm and slightly lower than 4% at other bands (Table 2). This high uncertainty at 412 nm is an extreme case, due to sensitivity of marine reflectance (see e.g. Figure 8 in Morel and Maritorena, 2001). If we consider that errors on the input parameters are random (around true pressure, ozone, chlorophyll, etc.), this error budget contains mainly (at first order) the random uncertainty, on punctual calibration points. However systematic input errors would produce systematic error on calibration coefficients. Hence the exact structure of input error should be assessed in future studies.

Table 2: Uncertainty budget of DIMITRI Rayleigh vicarious calibration coefficients, from sensitivity analysis, decomposed by sources. (*) comes from Hagolle *et al*. (1999)

Band	Ozone [*]	Wind [*]	Pressure [*]	Aerosol	Chlorophyll	Pixel	Total
412		0.5%	0.1%	1%	3.0%	1.3%	5.9%
443		0.5%	0.1%	1%	2.5%	0.7%	4.8%
490		1%	0.1%	1%	0.5%	0.1%	2.7%
510		1%	0.1%	1%	0.2%	0.7%	3.0%
560	0.5%	1.5%	0.1%	1%	0.5%	1.0%	4.6%
620		1.5%	0.1%	1%	0.2%	0.9%	3.7%

665		1.5%	0.1%	1%	0.1%	0.3%	3.0%

3.1.3 Tentative random/systematic uncertainty breakdown

Since vicarious calibration aims eventually at providing a unique set of coefficients, by averaging all targets, the uncertainty budget should rigorously be split into:

- The random uncertainty: its contribution to the averaged calibration coefficient goes down as more calibration points are considered
- The systematic uncertainty: its contribution remains the same whatever the number of points

No systematic source of error has been theoretically identified in previous uncertainty budget. Hence, we have tried to assess it experimentally, with real MERIS vicarious coefficients at SPG (most rigorous case study at present time due to knowledge of auxiliary data and proper radiative transfer LUT), as described in section 5.1. Let us note σ the standard-deviation of a single target coefficient, i.e. the random uncertainty, and $\sigma(\overline{RA})$ the standard-deviation after averaging N targets; one has

$$\sigma(\overline{RA}) = \frac{\sigma}{\sqrt{N}} \qquad (24)$$

Despite only few points are available (18, see section 5.1), we observe that the experimental dispersion on $\overline{RA}$ does not follow this shape when N varies from 2 to 18. Assuming that the observed dispersion can be understood as the mean square error (MSE), we have searched the bias and random uncertainty following this decomposition:

$$MSE(N) = Bias^2 + \left(\frac{\sigma}{\sqrt{N}}\right)^2 \qquad (25)$$

In practice this is realised through a linear fit on $MSE(N) * N$. In order to avoid any statistical artefact when increasing the sample from N=2 to 18, we order it randomly and average over a large number of realisations (10 000).

Results of bias and σ are provided on Figure 7, and compared with previous sensitivity uncertainty budget. They present a smooth variation with wavelength and are roughly of same order of magnitude, from 8% at 412 nm to 1% at 665 nm. Extrapolating these numbers on a large number of targets, i.e. decreasing at maximum the random contribution, results into a bias of less than 6%.
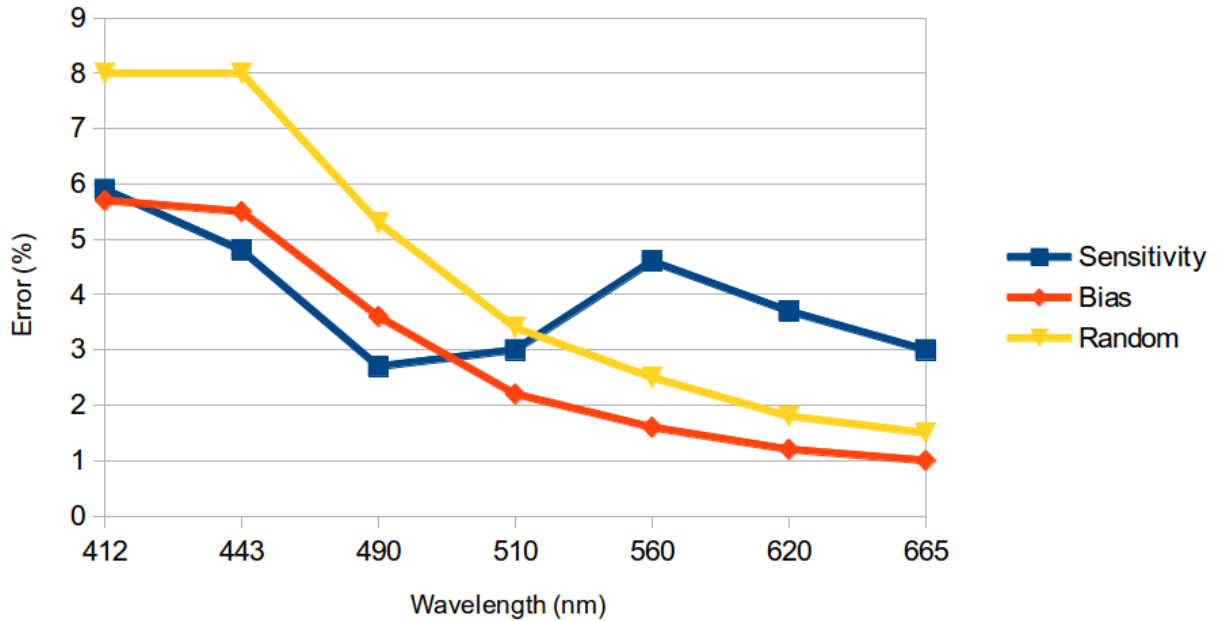
Figure 7 Tentative random (yellow)/bias(red) uncertainty breakdown of Rayleigh vicarious method, based on MERIS vicarious coefficients at SPG. Blue uncertainty is from the sensitivity study of section 3.1.2

The uncertainty budget derived here gives the overall accuracy of the method and should be improved. A way to derive a rigorous uncertainty budget would be to specify the random and systematic errors of each input parameter (e.g. chlorophyll, pressure, etc.) and to propagate both components into the methodology up to the simulated TOA reflectances. Such work is recommended for future DIMITRI releases.

4   Presentation of the implementation in DIMITRI_v4.x making use of Hyperspectral LibradTran LUTs and Hydrolight version 5.2 model

4.1   Radiative transfer Look up tables (LUT)

4.1.1   Format specification in DIMITRI

For every sensor (i.e. every set of wavelengths and spectral responses), DIMITRI Rayleigh calibration needs one Rayleigh LUT and four other LUT for each considered aerosol models: aerosol optical thickness dependence, downward total transmittance, upward total transmittance and path over Rayleigh fitting coefficients as function of optical thickness (previously noted XC in section 2.2.4).

All LUTs must be written in text file, with space as the field separator, following the naming convention of Table 3 to Table 7 below (AER may be any ASCII field identifying the aerosol model) and placed in directory AUX_DATA/RTM/SENSOR/. Any LUT satisfying this convention is detected by the GUI and can be used for the Rayleigh calibration. Reading and interpolation routines of DIMITRI_v3.0 are based on header description, giving size and discretisation of the LUT; this allows totally generic sampling in the LUT. Only the wavelengths must exactly follow those of the considered sensor, as defined in the Bin/DIMITRI_Band_Names.txt configuration file (NaN or any field may be used if some bands are not processed in the RTM).

Table 3: RHOR_SENSOR.txt template for Rayleigh reflectance LUT (MERIS example)

```
# MERIS Rayleigh Reflectance
# lambda:  412.0000  443.0000  490.0000  510.0000  560.0000  620.0000  665.0000  681.0000
708.0000  754.0000  761.0000  779.0000  865.0000  885.0000  900.0000
# thetas:   0.0000   10.2229   21.3480   32.4790   43.6114   54.7444   65.8776   77.0110
# thetav:   0.0000   10.2229   21.3480   32.4790   43.6114   54.7444   65.8776   77.0110
# deltaphi:   0.0000   30.0000   60.0000   90.0000  120.0000  150.0000  180.0000
# wind:   0.5000    7.0000
# tau550:   0.0000    0.0400    0.0600    0.1300    0.3300
# Inner loop is on tau550, wind, then deltaphi, thetav, thetas, and bands
# Dimensions:       15       8       8       7       2       5
     0.1254654675722122
…
```

Table 4: TAUA_SENSOR_AER.txt template for spectral dependence of aerosol optical thickness LUT at given AER model (MERIS example for MAR-99)

MERIS aerosol optical thickness for aerosol MAR99V

Columns gives tau_a corresponding to 7 reference optical thickness at 550 nm, see DIMITRI ATBD Methodology for Vicarious Calibration

(first optical thickness is zero)

lambda: 412.0000 443.0000 490.0000 510.0000 560.0000 620.0000 665.0000 681.0000 708.0000 754.0000 761.0000 779.0000 865.0000 885.0000 900.0000

Dimensions: 15   5

    0.0000000000000000   0.0511176362633705   0.0718025937676430   0.1442303806543350 0.3510798811912537

Table 5: TRA_DOWN_SENSOR_AER.txt template for downward total transmittance LUT at given AER model (MERIS example for MAR-99)

MERIS total downward transmittance (direct+diffuse, Rayleigh+aerosol) for aerosol model MAR99V

Columns gives t_up for 7 aerosol optical thickness (total, i.e. all layers) given in file TAUA_MERIS.txt

(first optical thickness is zero hence gives Rayleigh transmittance)

lambda: 412.0000 443.0000 490.0000 510.0000 560.0000 620.0000 665.0000 681.0000 708.0000 754.0000 761.0000 779.0000 865.0000 885.0000 900.0000

thetas: 0.0000 10.2229 21.3480 32.4790 43.6114 54.7444 65.8776 77.0110

Inner loop is on tau550, thetas, then on bands

Dimensions: 15   8   5

    0.8720846176147461   0.8649528622627258   0.8637801408767700   0.8601814508438110 0.8501554131507874

Table 6: TRA_UP_SENSOR_AER.txt template for upward total transmittance LUT at given AER model (PARASOL example for MAR-99)

MERIS total upward transmittance (direct+diffuse, Rayleigh+aerosol) for aerosol model MAR99V

Columns gives t_up for 7 aerosol optical thickness (total, i.e. all layers) given in file TAUA_MERIS.txt

(first optical thickness is zero hence gives Rayleigh transmittance)

lambda: 412.0000 443.0000 490.0000 510.0000 560.0000 620.0000 665.0000 681.0000 708.0000 754.0000 761.0000 779.0000 865.0000 885.0000 900.0000

thetav: 0.0000 10.2229 21.3480 32.4790 43.6114 54.7444 65.8776 77.0110

```
# Inner loop is on tau550, thetav, then on bands

# Dimensions:        15        8         5

     0.8720067739486694    0.8649499416351318    0.8637588024139404    0.8602198362350464
0.8503940701484680
```

Table 7: Structure of BRDF LUT for L_w / E_d(0+), i.e. ρ_w/π.

```
# standard test file lut

labels val lambda theta_s theta_v delta_phi wind chl

units val_units nm deg deg deg ms-1 mgm-3

# dimensions

47 9 9 24 3 21

# lambda (nm)

340 350 360 370 380 390 400 410 420 430 440 450 460 470 480 490 500 510 520 530 540 550 560
570 580 590 600 610 620 630 640 650 660 670 680 690 700 710 720 730 740 750 760 770 780 790
800

# theta_s (deg)

0 10 20 30 40 50 60 70 80

# theta_v (deg)

0 10 20 30 40 50 60 70 80

# delta_phi (deg)

0 15 30 45 60 75 90 105 120 135 150 165 180 195 210 225 240 255 270 285 300 315 330 345

# wind (ms-1)

0.5 7 15

# chl (mgm-3)

0.01 0.02 0.03 0.04 0.05 0.06 0.08 0.09 0.1 0.11 0.12 0.2 0.3 0.5 1 2 3 4 5 10 20

# data, from inner loop to outer: lambda, theta_s, theta_v, delta_phi, wind, chl

0.0110553 0.0143791 0.0160343 0.0181537 0.0165921 0.0182862 0.0195017 0.0212603 0.0196469
0.0170696  0.0135635  0.0100285  0.00903388  0.0080296  0.00658734  0.0054679  0.00402303
0.00249237    0.00187594    0.00165135    0.00141281    0.0011099    0.000946941    0.000788989
0.000573875  0.000357569  0.000204086  0.000161111  0.000145257  0.000129044  0.000111461
9.82883e-05   7.69498e-05   6.78898e-05   6.06776e-05   5.17965e-05   4.06505e-05   2.90872e-05
1.85966e-05 1.20997e-05 8.7023e-06 7.98704e-06 7.39099e-06 7.15257e-06 7.27178e-06 7.62941e-
06 7.62941e-06
```

Table 8: Structure of Rayleigh Optical thickness vs wavelength following Bodhaine et al., 1999.

```
# TAUR_BDHN99 AT LUT WAVELENGTH
# Dimensions:     147        2
     2.5314788818359375    -0.1471159062290361
```

4.1.2   Atmospheric radiative transfer LUTs generation

This section describes the generation of the look-up tables of atmospheric path reflectance, total transmission and relative optical thickness over wavelength as required by both the Rayleigh calibration and the sunglint calibration in DIMITRI. The look-up tables required are almost identical in structure to those used in the MERIS atmospheric correction scheme (Antoine and Morel 2011, Barker *et al*. 2012), but must be generated for every band of every sensor contained in DIMITRI. Currently these bands cover wavelengths from 340 nm to 5000 nm. While the Rayleigh correction requires wavelengths up to 700 nm, plus some in the NIR for aerosol detection, the glint calibration requires these tables at all wavelengths. Since many of the sensors in DIMITRI cover the same wavelength ranges the approach that has been taken is to produce one overall hyperspectral look-up table that can be convolved to each sensor band using the relative spectral response function (RSR) of each band. This approach makes the modelling more efficient and has the benefit that if new sensors are added to DIMITRI their Rayleigh and glint calibration look-up tables can be generated without further modelling, as long as the wavelengths are in the range 340 to 5000 nm.

4.1.3   Computational considerations

As the values required are for a Rayleigh scattering based calibration it is required to calculate them to the highest accuracy possible, which means they must be fully vectorial (with polarisation) since scalar modelling can introduce deviations of a few percentage in Rayleigh scattering (Hedley et al . 2013). Here, we have used a modified version of the libRadtran Monte Carlo model Mystic (Mayer and Kylling 2005; Mayer 2009). This model is capable of vectorial or scalar modelling and the vectorial mode Rayleigh scattering has been validated against both the MERIS atmospheric correction look-up tables and an independent model, Siro, developed at the Finnish Meterological Institute (Kujanpää 2013) (Figure 3).

The disadvantage of Mystic is that it is computationally slow, and being a Monte Carlo model is subject to statistical noise if insufficient computational effort is applied. In particular, with Mystic, each individual solar-view geometry requires a fully independent model run. Other models, such as the scalar Disort, can typically output results for a set of view zenith angles and relative azimuths for each run, but with Mystic one run must be done for every combination of solar, view and relative azimuth angles. These computational considerations are not trivial and require some compromises to be made. On a standard workstation, to produce results with the statistical

convergence shown in Figure 3 takes approximately 15 seconds per Mystic run on average (the run time increases with aerosol optical thickness). The MERIS atmospheric correction look-up tables are tabulated over 25 zenith angles, 23 azimuth angles, 3 wind speeds, 7 aerosol optical thicknesses. If tables were to be generated at this resolution at 400 wavelengths, for example, then the computation time would be 25 x 25 x 23 x 3 x 7 x 400 x 15 seconds = 57 years. Therefore a compromise has been made in terms of the angular resolution of the modelling (Table 8). Modelling at every nanometre is unfeasible so 386 wavelengths from 340 – 5000 nm have been chosen as outlined in Table 8. This wavelength choice means that even the narrowest bands, MERIS at 9 nm, will have a minimum of two tabulated values within their RSR, but most will have many more. Conversely for bands that are wide this method ensures they are based on results spread across the band width. For the structure in Table 8, running the look-up table generation on a high-end workstation where calculation can be parallelised in up to 12 concurrent processes enables a look-up table for one aerosol model to be generated in approximately 4 weeks of compute time.

Figure 8: Example Rayleigh scattering results from Hedley *et al*. (2013) at 443 nm, from the MERIS atmospheric correction look-up tables and from Mystic and Siro in spherical shell vectorial mode. *Left side*: Rayleigh scattering with error bars showing ±1 standard error on the mean for Mystic results. *Right side*: corresponding percentage difference between MERIS and Siro, and MERIS and Mystic. *Note:* both Mystic and Siro predict an error of only one third of a percent due to plane parallel versus spherical shell modelling at zero solar and zenith angles, hence this is not an explanation for the small deviations of 2 − 3% seen here.

4.1.4   Details of the required tables

The required tables are as follows:

1. Atmospheric path reflectance

This is calculated over a 'black ocean', i.e. the bottom boundary is a wind-blown air water interface but below surface reflection is zero. The direct reflectance path from the surface is excluded so that the reflectance represents photons that have undergone one or more atmospheric scattering events. To evaluate this requires a modification to the Mystic code to exclude photons that have not undergone an atmospheric scattering event. Note, gaseous absorption is also excluded in this calculation as this is corrected for elsewhere.

2. Total transmission, upward and downward

The product of the total transmission upward and downward is evaluated from Mystic using another modification that excludes photons that have not reflected from the bottom boundary.

The model is run over a Lambertian bottom of diffuse reflectance 0.1, the total transmittance is then the reflectance divided by 0.1 and corresponds to the assumption that water-leaving reflectance has a Lambertian BRDF. This assumption, while not strictly accurate (Morel and Gentili, 1993), will have minimal impact in this context. The assumption of Lambertian sub-surface reflectance has been shown to introduce only small errors (Yang and Gordon, 1997), see further discussion on this issue in Hedley *et al.* (2013). In addition the Lambertian assumption allows decoupling of the upward and downward transmittances, since the bottom boundary reflectance only has a dependence on the cosine of the solar zenith angle. The algorithm input requires that the upward and downward total transmittances be tabulated separately, although it is only their product that is used (Eqn. 13). If the model is run with a full set of solar zenith angles with view angle fixed (e.g. at zero) and vice versa the individual upward and downward transmissions could be calculated except there is unavoidably an unknown scaling factor between the upward and downward transmissions. In other words, for n zenith angles, there are $2n$ unknowns, but only $2n$-1 values to derive these from. This can be solved by assuming the upward and downward transmissions at zenith angle zero are equal. Note this is simply a trick to enable the algorithm implementation to be supplied with separate tables for upward and downward transmittance. When the product is formed the unknown factor disappears and the correct total transmission is used in Eqn. 12 regardless of this assumption.

This reflectance-based method for deriving the transmittance is required and appropriate because: 1) Mystic in general lacks outputs from which the total transmittances can be easily computed, and 2) it is the inverse of the process that must be captured, i.e. the reconstruction of the TOA reflectance from the bottom boundary reflectance (Eqn. 13). Decoupling of the water leaving reflectance from the atmospheric radiative transfer is equivalent to assuming that higher order photon interactions at the bottom boundary are negligible, i.e. that a photon reflects once only from the water body and hence the TOA reflectance is a linear function of the water body reflectance. This is valid, at least for diffuse reflectances up to 0.1, as shown in Figure 9 (see also Hedley *et al* 2013).
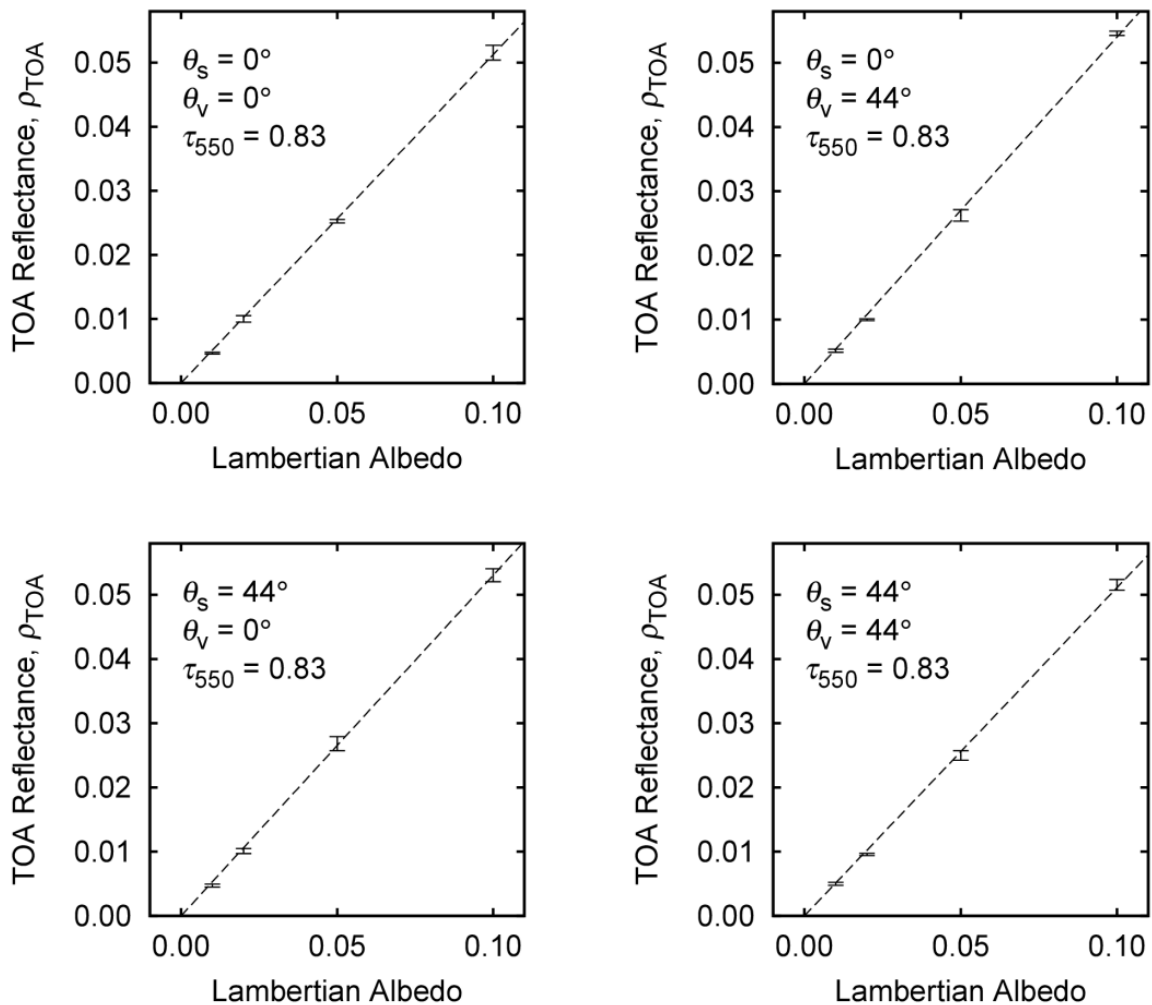
Figure 9: TOA reflectance from diffuse transmission paths as a function of bottom boundary Lambertian albedo from Hedley *et al*. (2013). These results were calculated in scalar spherical shell Mystic with the MAR-99 aerosol model (MERIS aerosol no. 4) τa (550) = 0.83, but the general conclusion of linearity with bottom reflectance will hold for plane parallel vectorial modelling. Error bars are ± 1 standard error on the mean, line is least squares linear fit.

3. Variation in optical thickness with band

The radiative transfer models are run with aerosol models of differing specified optical thicknesses at wavelength 550 nm. The algorithms require that the corresponding aerosol optical thickness can be derived for other bands. This table enables that transformation to be made, for a given sensor and aerosol model it relates the optical thickness in one band to the others. These values are not dependent on solar-view geometry or wind speed. The values at each wavelength are output directly in the libRadtran run log at each wavelength. The values for each sensor band

are derived from the convolution by the sensor RSR.

4.1.5   Details of libRadtran parameterisation

Certain details of the libRadtran parameterisation are listed below for reference. The next section describes the aerosol models.

- Standard US atmosphere 'AFGLUS'
- Atmospheric height 120 km
- Pressure 1013 mb
- No gaseous absorption
- Plane parallel configuration
- Vectorial scattering
- For black ocean, vectorial Mischenko & Travis wind-blown sea surface including the correction introduced after libRadtran version 1.7

Mystic can also be run in spherical shell mode, and even for solar and zenith angles of zero this can make a third of a percentage difference in the Rayleigh scattering, and for other solar-view geometries the deviation can rise to several percent (Hedley *et al*. 2013). While the LUT generation code permits switching to spherical shell mode, within the context of this project the 'traditional' plane parallel assumption has been made.

Testing indicated that the Mystic options for forward or backward ray tracing and the 'vroom' optimisation did not reduce processing time or produce any overall improvement in statistical convergence. The 'escape' photon optimisation was enabled throughout.

Table 9: Structure of look-up tables for one aerosol model.

Parameter	Units	n	Values
λ	nm	147	340 to 1000 with step 10 (67), 1050 to 5000 step 50 (80)
θ_s	deg.	8	0, 10.2229, 21.3480, 32.4790, 43.6114, 54.7444, 65.8776, 77.0110
θ_v	deg.	8	0, 10.2229, 21.3480, 32.4790, 43.6114, 54.7444, 65.8776, 77.0110
$\Delta\phi$	deg.	7	0, 30, 60, 90, 120, 150, 180
wind	ms^{-1}	2	0.5, 7
$\tau_a(550)$	-	5	0, 0.04, 0.06, 0.13, 0.33
	total:		658560

Table 10: Components used in OPAC aerosol models as implemented in libRadtran (Hess *et al.* 1998)

Code	Meaning
inso	insoluble
waso	water_soluble
soot	soot
ssam	sea_salt_accumulation_mode
sscm	sea_salt_coarse_mode
minm	mineral_nucleation_mode
miam	mineral_accumulation_mode
micm	mineral_coarse_mode
mitr	mineral_transported
suso	sulfate_droplets

4.1.6 Aerosol models

Since generating a table for one aerosol model takes approximately 4 weeks of compute time, it has been restricted to only one aerosol model to the algorithm.

- **MAR99:** the MERIS atmospheric correction aerosol model no. 4

Details of the aerosol model parameterisations are given in the following two sections. Figure 10 shows aerosol optical thicknesses as a function of wavelength for different models, as output by LibRadtran, and indicates that MAR50 and MAR99 are correctly set-up as corresponding to the MERIS atmospheric correction LUT models. Interestingly although the OPAC model MC50 is described as corresponding to 50% relative humidity in the LibRadtran documentation, it corresponds closely to MAR99, which is considered as 99% relative humidity. However the slope of MC50 starts to deviate in the Near-Infra Red, so it is worthwhile to retain it in the algorithm. MAR50 and MAR99 represent the extreme slopes in optical thickness from the MERIS maritime aerosol models, so candidate models for future inclusion might be MAR70 and MAR90 which represent intermediate slopes.
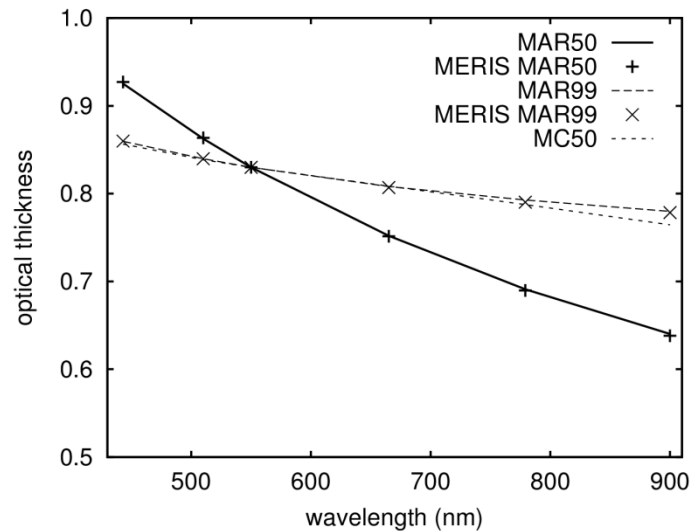
Figure 10: Aerosol optical thickness from 440 to 900 nm for the implemented aerosol models MAR50, MAR99 and MC50. Tabulated values for MAR50 and MAR99 from the MERIS atmospheric correction algorithm are also shown as point data.

MAR99, the MERIS atmospheric correction models

The model has been constructed for use in vectorial mode Mystic by use of the mie scattering tool supplied with libRadtran. The size distributions and refractive indices of the model components used are specified in the MERIS RMD and original paper by Shettle and Fenn (1979). The mie tool is used to generate the wavelength dependent Mueller matrices and single scattering albedos, and these are conveniently output in netCDF files that libRadtran takes as input. An additional input file specifies the vertical profiles of the differing aerosol components, which for these models occur in three distinct layers, 0 -2 km, 2 -12 km and 12 – 50 km. Again, the relative proportions were fixed according to the values in the MERIS RMD (Barker *et al*. 2012), but the 0 - 2 km fraction was scaled to reach the required $\tau_a(550)$ values as in Table 8.. The models were validated by checking the relative optical thicknesses at different wavelengths to those tabulated in the MERIS RMD. Barring numerical differences in the modelling and undocumented details in the parameterisation, the MAR99 model should correspond exactly to hyperspectral versions of model 4 in the MERIS atmospheric correction.

4.2 Auxiliary data for marine modelling

Pure seawater absorption and scattering coefficients come from the NASA ocean color repository: http://oceancolor.gsfc.nasa.gov/DOCS/RSR/water_coef.txt.

The table of averaged cosine for downwelling reflectance (μ_d in Morel (1988) and Morel and

Maritorena (2001)) comes from Morel *et al*. (2006) available on LOV repository at oceane.obs-vlfr.fr/pub/morel. Other parameters of the Morel and Maritorena (2001) model are directly taken from their table 2.

Refractive index of pure seawater comes from MERIS tables (Barker *et al*. 2012) and is spectrally interpolated for any wavelength.

As suggested by the sensitivity analysis, deriving meaningful coefficients needs the most realistic chlorophyll estimate. The ESA GlobColour project (http://www.globcolour.info) provides several ocean colour products derived from the merging of SeaWiFS, Aqua-MODIS and MERIS water leaving radiance data. The dataset covers the period 1998-2012. The dataset used in DIMITRI is the so-called Chl1-GSM product, at 0.25 degree spatial resolution (Bouvet 2013). The merging of the three sensor data is done by minimizing the difference between the individual sensor water leaving radiances and the water leaving radiance predicted by a bio-optical model. The minimization process leads to the retrieval of the bio-optical model parameters, one of which is the chlorophyll-a concentration. The bio-optical model is the so-called GSM model (Maritorena et al. (2002) and Maritorena et al. (2005)). The monthly climatology Chl1 values averaged over the optimum regions of interest are computed. Note that users can still add any chlorophyll climatology file, which would be automatically processed by DIMITRI.
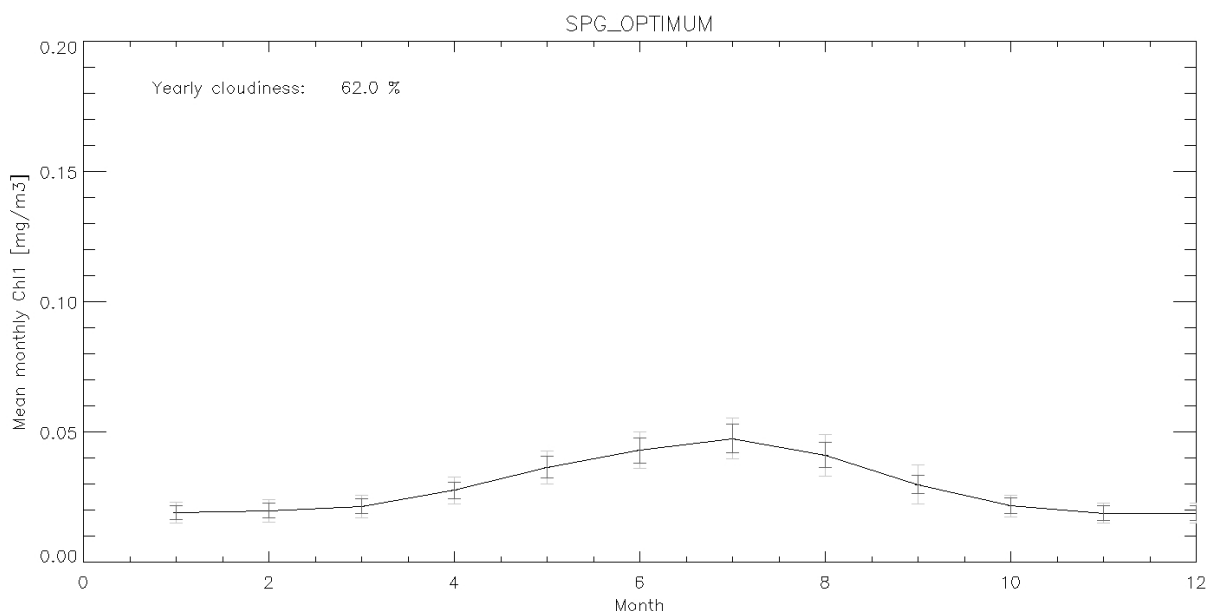

Figure 11: The monthly variations of the Chl1 climatology $CHL1_{Clim}(month)$ derived from the full period 1998-2012 over SPG-optimum for applying the Raleigh scattering methodology. The black error bar is the associated uncertainty which the $CHL1\_uncertainty_{Clim}(month)$ and the grey error bar is the $CHL1\_stddev_{Clim}(month)$.

4.3   Output files generated by the Rayleigh calibration

Five types of files are systematically generated for each Rayleigh vicarious calibration run:

1. **RAYLEIGH_CAL_LOG.txt:** log file summarising all options of the run (parameters).

2. **SITE_SENSOR_PROC_RAYLEIGH_ARG_YYYYMMDD_hhmm.nc:** NetCDF file storing array REF_TO_SIM per band per pixel over the ROI

3. **SITE_SENSOR_PROC_RAYLEIGH_ARG_YYYYMMDD-hhmm_DIR_BAND.JPG**: scatter-plot of the simulated reflectance to the observed one; and an histogram of the ratio observed-to-simulated one per band per acquisition.

4. **SITE_SENSOR_PROC_RAYLEIGH_ARG_YYYYMMDD-hhmm_PERIOD.csv:** A csv format file storing the time-series of the calibration ratio over the analysed period.

5. **SITE_SENSOR_PROC_RAYLEIGH_ARG_YYYYMMDD-hhmm_DIR_BAND_PERIOD.JPG:**   A plot of the time-series of the ratios per direction per band over the analysed period.

4.4   DIMITRI modules/functions/architecture

The Rayleigh calibration methodology is implemented as an individual IDL module, called by a new GUI module (or directly in command line); it then calls several separated routines for specific jobs (e.g. computation of Rayleigh reflectance, of marine models, etc.). All routines related to the Rayleigh vicarious calibration are stored in the Source/calibration_ARG directory.

Schematically, the main Rayleigh calibration module:

- Interfaces with the DIMITRI database to identify appropriate L1b extractions with respect to chosen region, sensor, processing version and year;
- Screens data for ROI cloud and region coverage; in the pixel-by-pixel mode, pixels are further screened by the cloud mask;
- Finds all pixels within other user defined parameters specific to the calibration method;
- Reads all RTM LUT;
- Performs the Rayleigh Calibration band per band;
- Post-processed the coefficients (averaged, statistics);
- Outputs the individual and averaged calibration coefficients for each band in several text and image file, as defined in section 4.3.
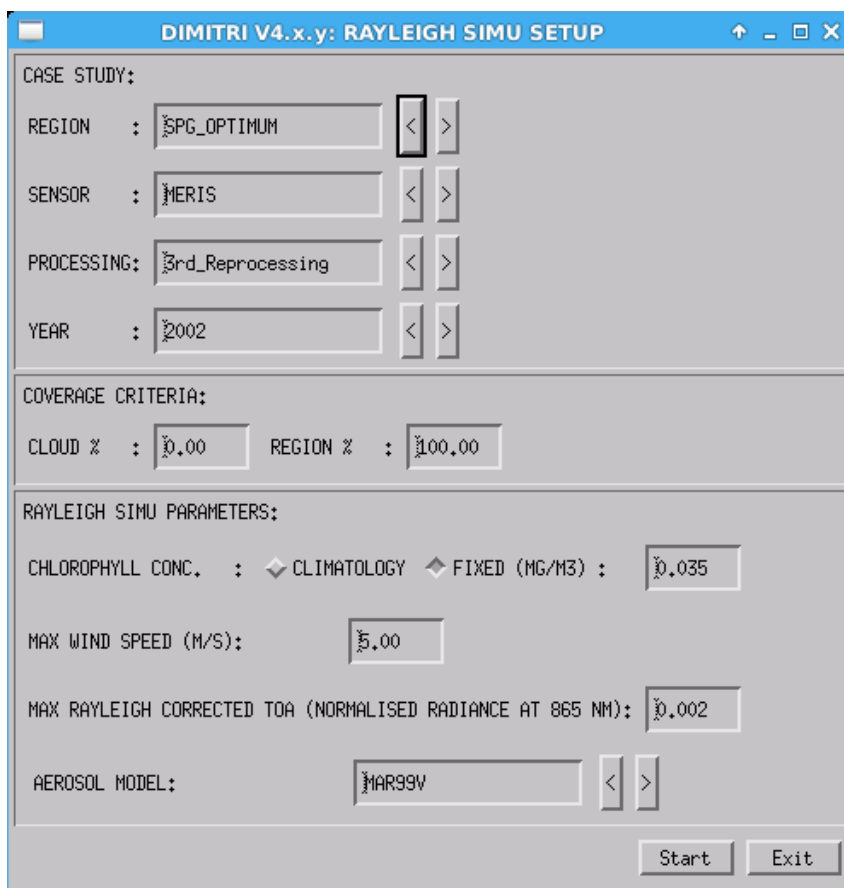
4.5   HMI updates and User options

The Rayleigh calibration methodology allows both GUI and command line activation. The Rayleigh set-up GUI from DIMITRI_v4.x.y displayed on Figure 12.
All processing parameters specific to the Rayleigh calibration are selectable by the user through

the GUI window:

- Case study (region, sensor, processing version, year, output directory);
- Cloud and region coverage percentage; note that scenes having a manual cloud screening set to 0 will be selected whatever the automated cloud screening value;
- Chlorophyll concentration, either by monthly climatology put in the DIMITRI auxiliary folder or by a fixed values;
- Maximum wind speed;
- Maximum Rayleigh corrected normalised radiance at 865 nm;
- Aerosol model, among an automated list built on all models existing in DIMITRI auxiliary folder, sensor per sensor.

Figure 12: DIMITRI_v4.x.y window for parameterising the set-up of Rayleigh scattering vicarious calibration

5   Results and implementation comparisons

Note: Wind speed modulus and gas concentrations used for atmospheric quantities computation come from DIMITRI auxiliary data associated to each measurement, as stored in SENSOR_TOA_REF.dat files. Because current DIMITRI version only provides these auxiliary data for MERIS, default values of w_m=5m/s and O_3=300 DU are automatically selected in order to present results for all sensors.

In all the following results default options of the Rayleigh calibration are used, unless otherwise specified:

- 0% ROI cloud coverage,
- 100% ROI coverage,
- Maximum wind modulus of 5 m/s,
- Threshold of 0.002 on normalised Rayleigh corrected radiance at 865 nm and
- MAR-99 aerosol model.

The chlorophyll concentration comes from previously detailed climatology.

5.1   DIMITRI implementation results for MERIS

The mean coefficients over SPG for MERIS 3rd reprocessing, detailed in Table 11and plotted against wavelength on Figure 13 present a time-series of band 3 and 7 respectively. The results display biases of about +4% at 412 nm to -2% at 665 nm and the standard deviation is quite large, up to 10%.. –However, due to a relaxed RCNR865 (of 0.02) might lead to such results, and one cannot draw a clearer.

The time-series (Figure 13) does not show temporal trends, although the few numbers of points does not allow drawing a statistically robust conclusion. The results from SPG site are in good agreement with SIO ones (Figure 14), which probably indicates that the water leaving reflectance model needs more investigations to understand its impact on the calibration coefficients.

Table 11: MERIS 3rd reprocessing Rayleigh calibration coefficients over SPG

Band (nm)	Median DAk	Standard deviation	Mean uncertainty	N
412.00	1.035	0.009	0.041	28
443.00	1.057	0.011	0.042	28
490.00	1.041	0.012	0.041	28
510.00	1.009	0.012	0.040	28
560.00	0.994	0.013	0.039	28
620.00	0.980	0.012	0.039	28
665.00	0.982	0.012	0.039	28
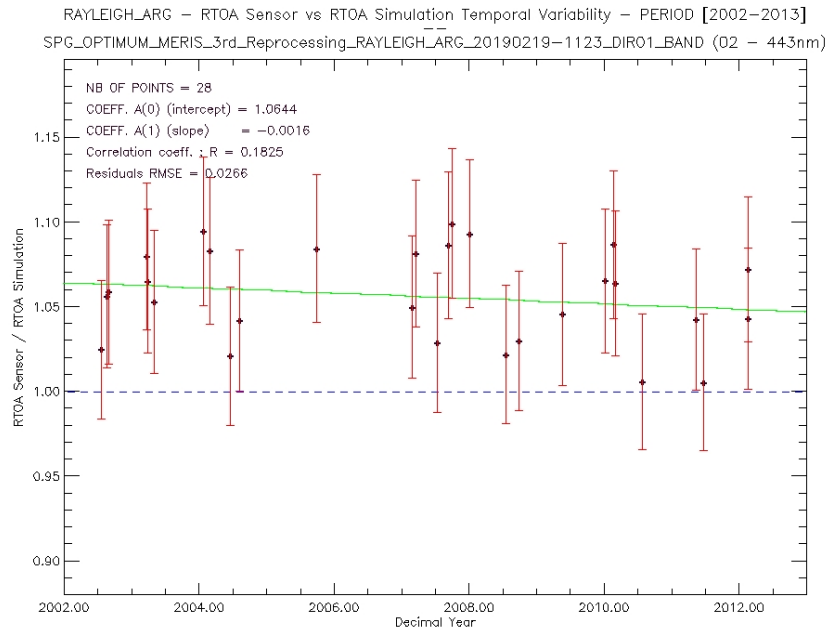
Figure 13 Time-series of (top) band-2 and (bottom) band-7 from MERIS 3rd reprocessing Rayleigh calibration coefficients as ratios TOA-Sensor/TOA-Simulation over SPG-OPTIMUM, Error bars are method's uncertainty.
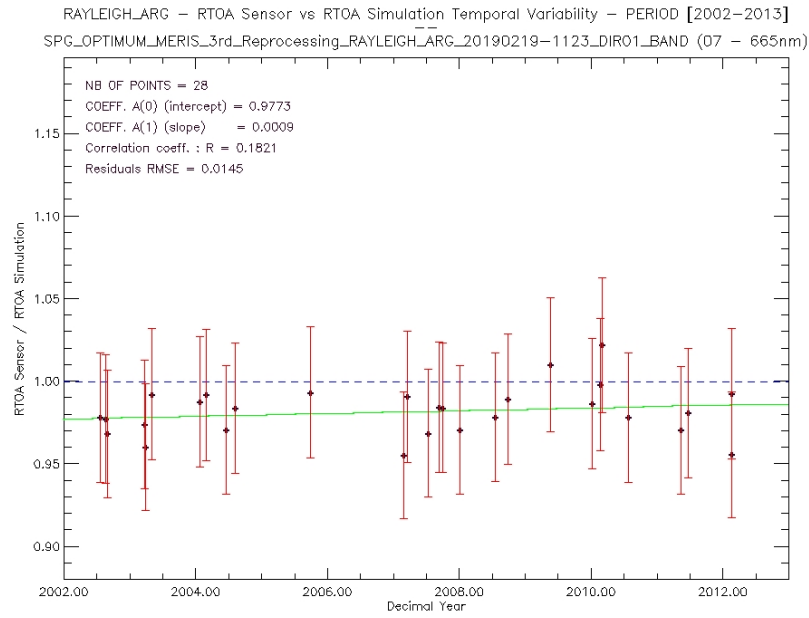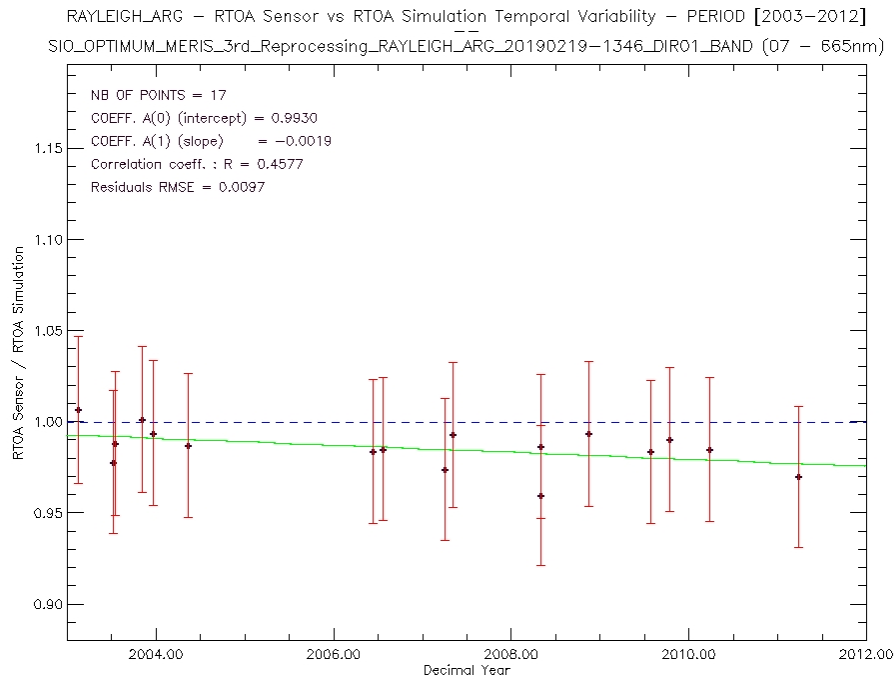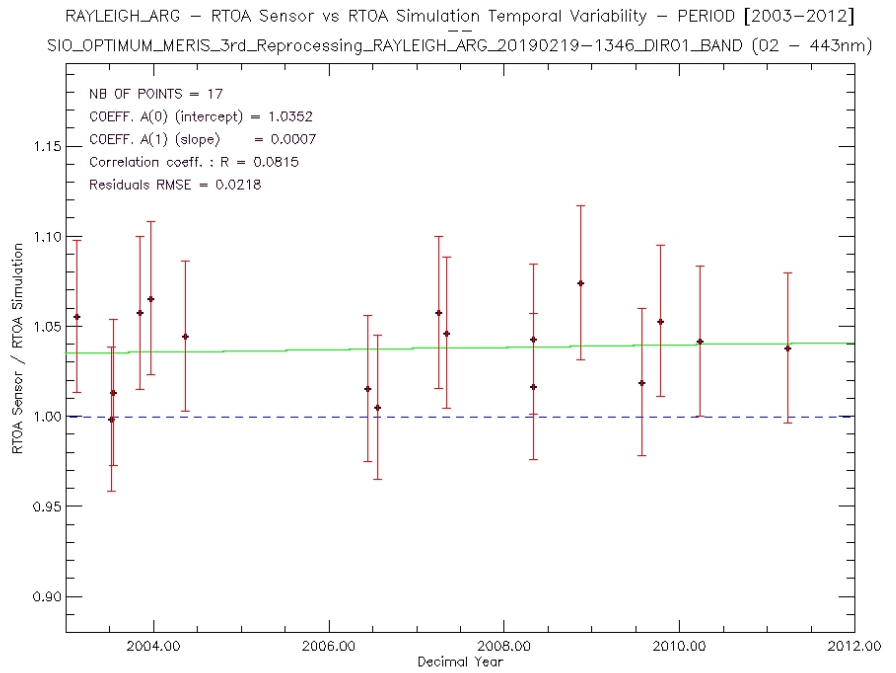
Figure 14: Time-series of (top) band-2 and (bottom) band-7 from MERIS 3rd reprocessing Rayleigh calibration coefficients as ratios TOA-Sensor/TOA-Simulation over SIO-OPTIMUM, Error bars are method's uncertainty.

5.2 DIMITRI implementation results for other sensors

Rayleigh calibration coefficients over SPG for AATSR 3RP are displayed on Figure 15 . AATSR presents larger standard-deviations, which is possibly due to the averaging multi-directional views in single observations.

Table 12: AATSR 3rd reprocessing Rayleigh calibration coefficients over SPG (Nadir view)

Band (nm)	Median Ak	Standard-deviation	Mean uncertainty	N
555.00	1.013	0.014	0.04	13
666.00	0.993	0.015	0.04	13

Table 13: AATSR 3rd reprocessing Rayleigh calibration coefficients over SPG (Forward view)

Band (nm)	Median Ak	Standard-deviation	Mean uncertainty	N
555.00	1.007	0.011	0.04	14
666.00	1.004	0.011	0.04	14

RAYLEIGH_ARG − RTOA Sensor vs RTOA Simulation Temporal Variability − PERIOD [2002−2012]
SPG_OPTIMUM_AATSR_3rd_Reprocessing_RAYLEIGH_ARG_20190317−1440_DIR01_BAND (01 − 555nm)
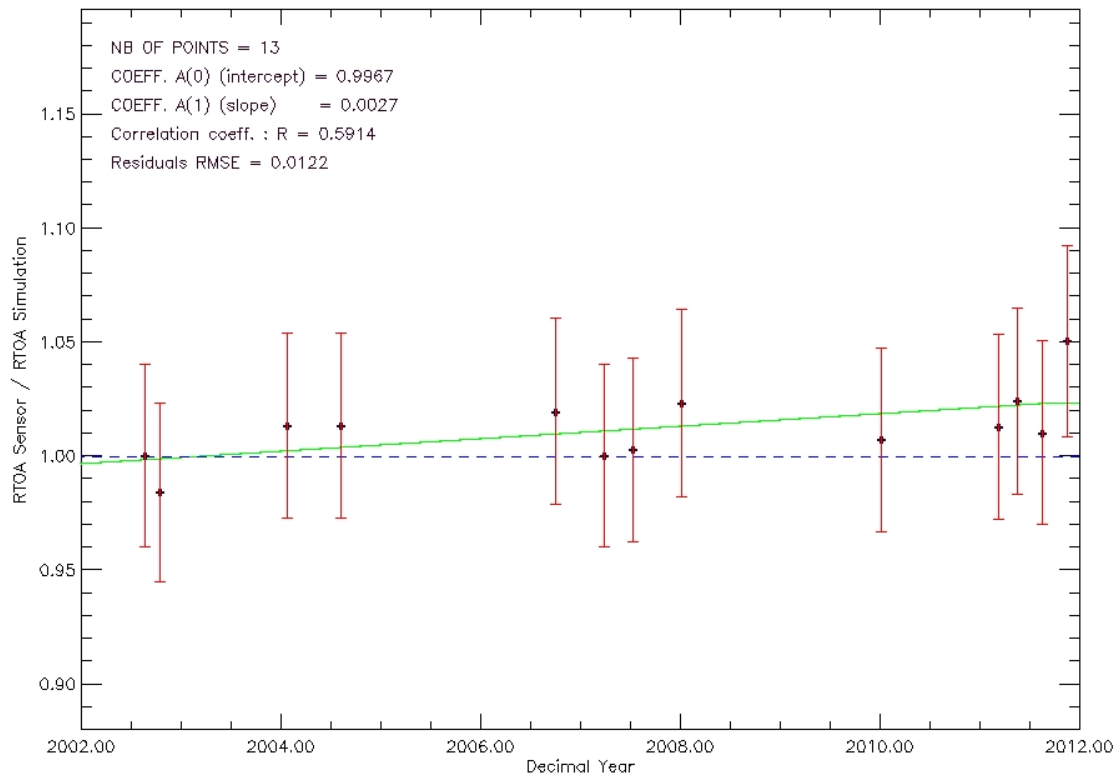
NB OF POINTS = 13
COEFF. A(0) (intercept) = 0.9967
COEFF. A(1) (slope)   = 0.0027
Correlation coeff. : R = 0.5914
Residuals RMSE = 0.0122

RAYLEIGH_ARG — RTOA Sensor vs RTOA Simulation Temporal Variability — PERIOD [2002−2012]
SPG_OPTIMUM_AATSR_3rd_Reprocessing_RAYLEIGH_ARG_20190317−1440_DIR01_BAND (02 − 660nm)
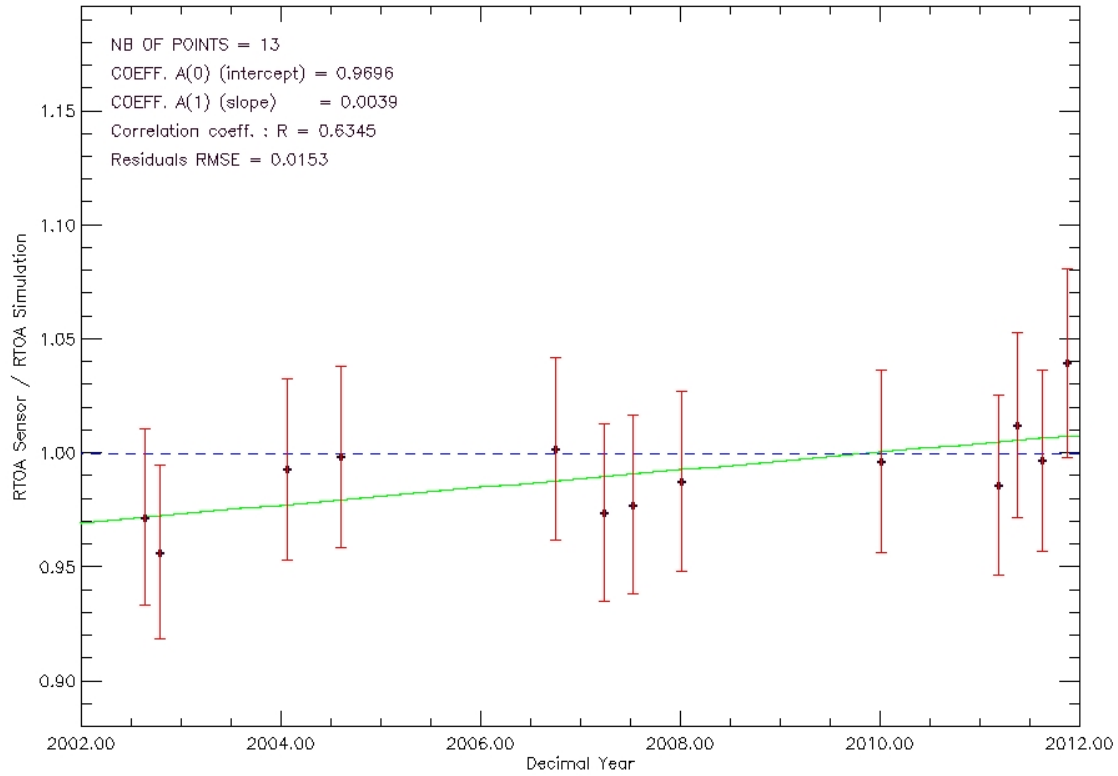
NB OF POINTS = 13
COEFF. A(0) (intercept) = 0.9696
COEFF. A(1) (slope) = 0.0039
Correlation coeff. : R = 0.6345
Residuals RMSE = 0.0153

RAYLEIGH_ARG — RTOA Sensor vs RTOA Simulation Temporal Variability — PERIOD [2002—2012]
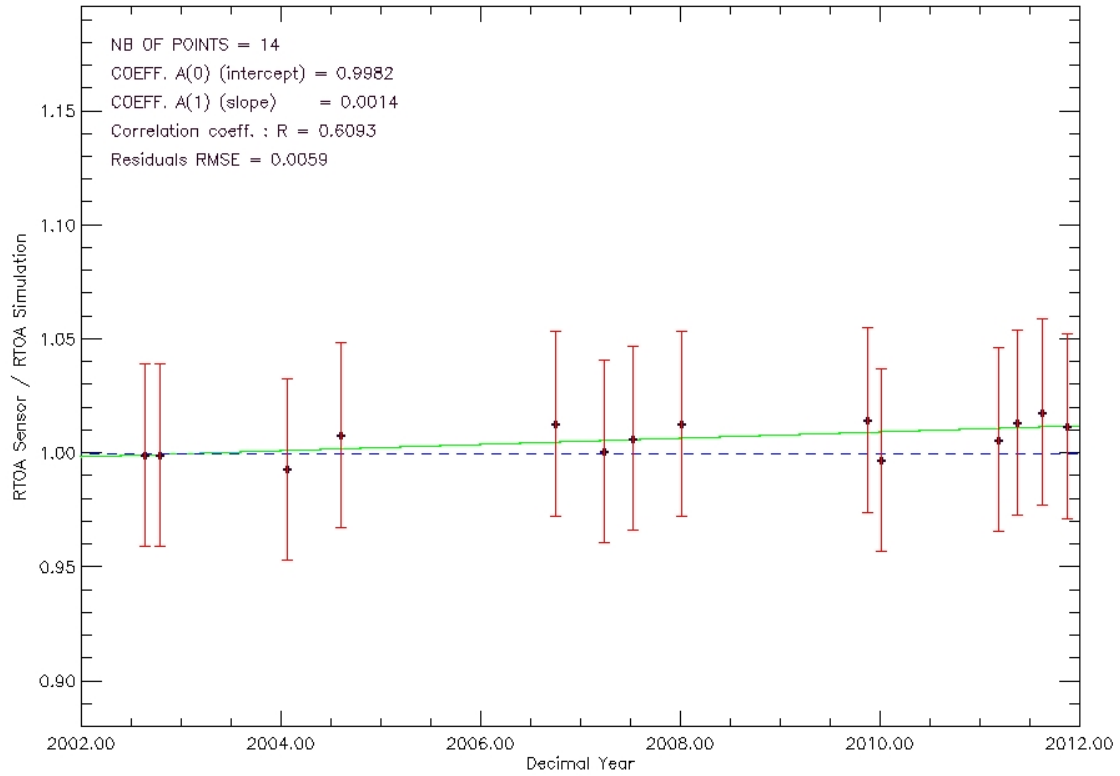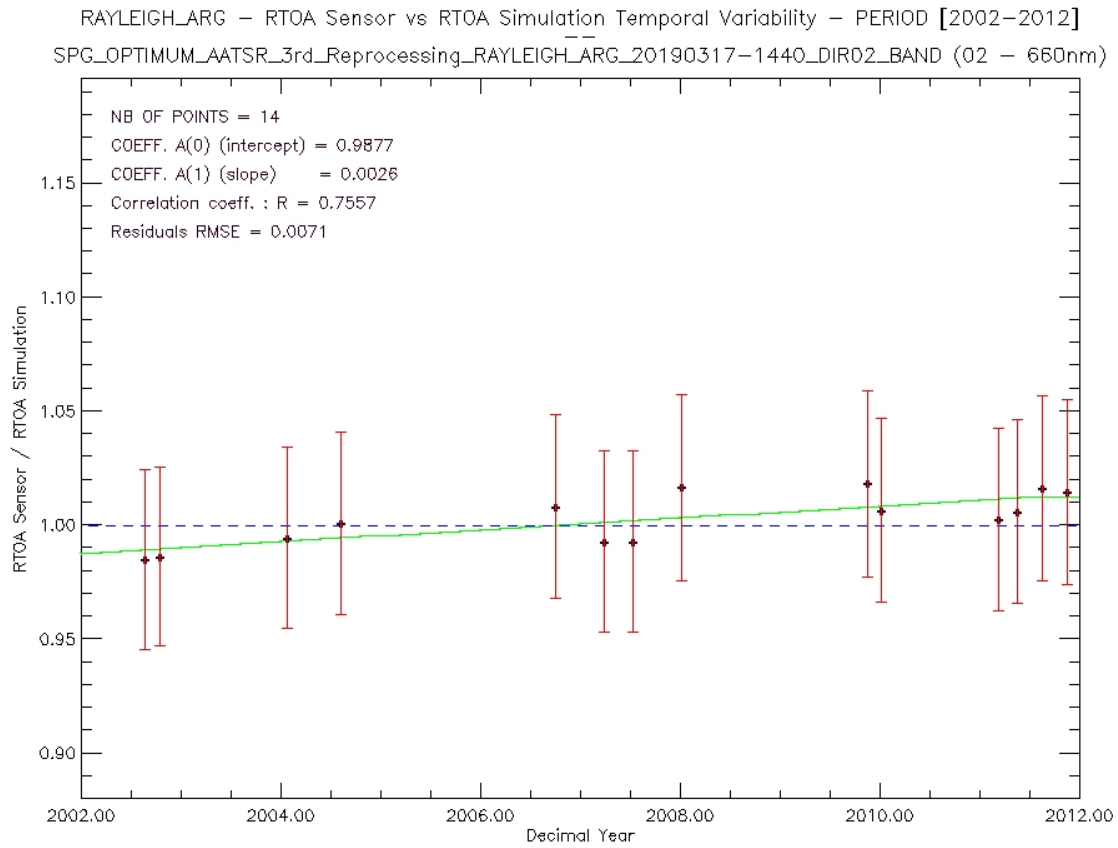SPG_OPTIMUM_AATSR_3rd_Reprocessing_RAYLEIGH_ARG_20190317—1440_DIR02_BAND (01 — 555nm)

Figure 15: Time-series of (top to bottom) of band-1 and band-2, Nadir and Forward (respectively) from AATSR 3rd reprocessing Rayleigh calibration coefficients as ratios TOA-Sensor/TOA-Simulation over SPG-OPTIMUM, Error bars are method's uncertainty.

6 Discussion and conclusion

The Rayleigh calibration method implemented in DIMITRI_v3.0 follows essentially the initial work of Hagolle *et al*. (1999), with several adaptations taking into account more recent and well-tried ocean colour modelling in marine reflectance and aerosol contribution.

Several improvements have been carried out on the Rayleigh calibration method in the current DIMITRI v4.x.y version such as:

- Implementing a new hyperspectral LUTs for the aerosol and atmospheric reflectance.
- Implementing the atmospheric pressure adjustment following Bodhaine et al. 1999.
- Implementing hyperspectral LUTs of the water leaving reflectance taking in account the BRDF effects.

The DIMITRI_v4.x.y HMI allows users to easily choose all main parameters of the calibration (thresholds, chlorophyll concentration, aerosol model, etc.). Automated handling of auxiliary files also gives users the possibility to immediately test other parameterisations of the signal modelling, both for the marine contribution (e.g. chlorophyll climatology, coefficients of the Morel and Maritorena (2011) model) and atmospheric component (e.g. new look-up tables with different geometrical discretisation or aerosol models).

Vicarious coefficients presented here for MERIS and AATSR are slightly different from the previous ones in DIMITRI v3.x.y, thus more analysis of the results is recommended.

7 References

Antoine, D. and A. Morel (1999). A multiple scattering algorithm for atmospheric correction of remotely-sensed ocean colour (MERIS instrument): principle and implementation for atmospheres carrying various aerosols including absorbing ones, IJRS, 20, 1875-1916.

Antoine, D. and Morel, A. (2011). MERIS ATBD 2.7 Atmospheric Correction of the MERIS observations Over Ocean Case 1 waters. Technical Report MERIS ATBD 2.7 v5.1-July2011 (Version 5.1).

Barker, K., Antoine, D., Bourg, L., Brockmann, C., Doerffer, R., Fischer, J., Moore, G., Santer, R., and Zagolski, F. (2012). Reference Model for MERIS Level 2 Processing. Third MERIS reprocessing: Ocean Branch. Technical Report PO-TN-MEL-GS-0026 (Version 5.2)

Bourg, L. and S. Delwart (2012) MERIS instrument calibration. Available at http://earth.eo.esa.int/pcs/envisat/meris/documentation/

Bouvet, M. (2006). Intercomparisons of imaging spectrometers over the Salar de Uyuni (Bolivia). *Proc. 2nd MERIS and AATSR Calibration and Geophysical Validation Meeting (MAVT-2006)*, 20-24 March 2006, ESRIN.

Bouvet, M. (2011). Simulation of VEGETATION measurements with DIMITRI. ESA Tech. Note: TEC-EEP/2011.713/MB

Bouvet, M. (2013) Selection of optimum oceanic sites for applying the Rayleigh scattering methodology to optical space sensors. ESA Technical Note, 06/12/2013.

Bouvet M., Goryl P., Chander G. Santer R., and Saunier S. (2007). Preliminary radiometric calibration assessment of ALOS AVNIR-2. Proc. Geoscience and Remote Sensing Symposium, IGARSS 2007

Bouvet M, Radiometric comparison of multispectral imagers over a pseudo-invariant calibration site using a reference radiometric model, Remote Sensing of Environment 140 (2014) 141–154

Cox, C., and W. Munk (1954), Statistics Of The Sea Surface Derived From Sun Glitter, J. Mar. Res., 13, 198 – 227

Fournie, B., Patrice Henry, P., Morel, A., Antoine, D., Montagner, F. (2002). Identification and characterization of stable homogenous oceanic zones: climatology and impact on in-flight calibration of space sensors over rayleigh scattering. Ocean Optics XVI, Santa Fe, NM.

Fougnie, B., Bracco, G., Lafrance, B., Ruffel, C., Hagolle, O., Tinel, C. (2007) PARASOL in-flight calibration and performance, Applied Optics, Vol. 46, No 22, 5435-5451

Fougnie, B., Henry, P., Lachérade, S., and P. Gamet (2012) Radiometric calibration of desert sites and oceanic target. Sentienl-3 calibration and validation planning meeting, ESA/ESRIN, March 2012.

Hagolle *et al*. (1999) Results of POLDER in-flight Calibration, IEEE Transactions on Geoscience and Remote Sensing, May 1999, Volume 37, Number 03

Hansen, J.E. and L. Travis, 1974. Light scattering in planetary atmospheres, Space Science Reviews, 16: 527-610.

Hedley (2017), QA4EO DIMITRI Evolution LUT description and use, Ref: ARG_DIM_QA4EO_LUT_SUM, 8th, Feb. 2017.

Hedley (2018), Pressure, latitude and C02 adjustments, Ref: ARG_DIM_QA4EO_ATM, 18 Jan. 2018.

Hedley (2019), Water-leaving reflectance BRDF, Ref: ARG_DIM_QA4EO_WL_BRDF, 26th Feb. 2019.

Hedley J, Lamquin N, Mazeran C. (2013) Atmoshperic Correction for Ocean Colour in a Spherical Shell Atmosphere. Algorithm Theoretical Basis Document. ESA Report GEOHR-D6 AO/1-7084/12/NL/AF (Version 0.9.2).

Hess M, Koepke P, Schult I (1998) Optical Properties of Aerosols and Clouds: The software package OPAC. Bulletin of the American Meteorological Society 79(5) 831-844.

Kay, S., Hedley, J., Lavender, S., and Nimmo-Smith, A. (2011). Light transfer at the ocean surfacemodelled using high resolution sea surface realizations. Opt. Express, 19(7):6493–6504.

Kou, L., D. Labrie, P. Chylek, 1993, "Refractive indices of water and ice in the 0.65-2.5 m spectral range," Appl. Opt.,32, 3531-3540 (1993).

Kujanpää, J. (2013). Atmospheric Correction for Geostationary High Resolution Ocean Applications (GEO-HR). Forward Model Description. Technical Report ESA Report GEOHR-D2 AO/1-7084/12/NL/AF (Version 1.1).

Lerebourg, C., Mazeran, C., Huot, J-P., Antoine, A. (2011) Vicarious adjustment of the MERIS Ocean Colour Radiometry. MERIS ATBD 2.24, Issue 1.0

Mayer, B. (2009). Radiative transfer in the cloudy atmosphere. EPJ Web of Conferences, 1:75–99.

Mayer, B. and Kylling, A. (2005). Technical note: The libradtran software package for radiative transfer calculations - description and examples of use. Atmospheric Chemistry and Physics, 7:1855–1877.

MERIS Level 2 Detailed Processing Model, June 2011, ref. PO-TN-MEL-GS-0006, Issue 8.0B available at http://earth.eo.esa.int/pcs/envisat/meris/documentation

M. I. Mishchenko and L. D. Travis, Satellite retrieval of aerosol properties over the ocean using polarization as well as intensity of reflected sunlight. J. Geophys. Res. 102, 16989-17013 (1997).

Mobley CD, Sundman L (2013) Hydrolight 5.2 User's Guide. Sequoia Scientific. Available online: http://www.sequoiasci.com/products/Hydrolight.aspx

Mobley CD, Gentili B, Gordon HR, Jin Z, Kattawar GW, Morel A, Reinersman P, Stamnes K, Stavn RH (1993) Comparison of numerical models for computing underwater light fields. Applied Optics 32(36), 7484-7504.

Morel, A. (1988). Optical modeling of the upper ocean in relation to its biogenous matter content (case 1 water), Journal of Geophysical Research, 93, 10,749-10,768.

Morel, A., and S. Maritorena (2001). Bio-optical properties of oceanic waters: A reappraisal. Journal of Geophysical research, 106, 7763-7780

Morel, A., and B. Gentili (1996). Diffuse reflectance of oceanic waters. 3. Implication of bidirectionality for the remote-sensing problem. Applied Optics, 35, 4850-4862.

Morel, A. and Gentili, B. (1993). Diffuse reflectance of oceanic waters. ii bidirectional aspects.Applied Optics, 32(33):6864–6879.

Morel, A., Gentili, B., Chami, M., and J. Ras (2006) Bio-optical properties of high chlorophyll Case1 waters and of yellow-substance-dominated Case2 waters. Deep-Sea Res. I, 53, 1439-1559

Pope, R. M. and E. S. Fry, 1997, "Absorption spectrum (380-700 nm) of pure water. II. Integrating cavity measurements," Appl. Opt.,36, 8710-8723.

Shettle, E.P. and R.W. Fenn, 1979. Models for the aerosols of the lower atmosphere and the effects of humidity variations on their optical properties. Environmental Research Papers, AFGL-TR-79-0214, 20 September 1979, AFGL, Hanscom (Mass.).

Smith, R.C. and K.S. Baker, 1981, "Optical properties of the clearest natural waters (200-800 nm)," Appl. Opt.,20, 177-184.

Vermote, E., R. Santer, P.Y. Deschamps and M. Herman, In-flight Calibration of Large Field-of-View Sensors at Short Wavelengths using Rayleigh Scattering, Int. Journal of Remote Sensing, 13, No 18, 1992. http://www.tandf.co.uk/journals/tres

Yang, H. and Gordon, H. R. (1997). Remote sensing of ocean color: assessment of water-leaving radiance bidirectional effects on atmospheric diffuse transmittance. Applied Optics, 36(30):7887–7897.

Zagolski, F. (2010) Specification of the Contents of the MERIS Radiative Transfer Tools used to Generate the Level-2 Auxiliary Data Products. Doc PO-RS-PAR-GS-0003, issue 4.A

DIMITRI_v4.x ATBD
Rayleigh Scattering Methodology for Vicarious Calibration

Reference: ARG_DIM_QA4EO - TN-004b
Revision: 2.1
Date: 26/09/2019
Page: 51

[End of Document]